Department of Precision and Microsystems Engineering

Ice-induced vibrations of wind turbines with a jacket support structure

Irene Marsman

Report no : 2018.041
Coach : Ir. Tom Willems
Professor : Prof. dr. P.G. Steeneken
Specialisation : Engineering Mechanics
Type of report : MSc Thesis
Date : December 3, 2018

TU Delft Delft University of Technology

Challenge the future

Ice-induced vibrations of wind turbines with a jacket support structure

Master of Science Thesis

For the degree of Master of Science in Precision and Microsystems Engineering at Delft University of Technology

Irene Marsman

December 3, 2018

Supervisors:	Prof. dr. P.G. Steeneken	Delft University of Technology
	Dr. ir. H. Hendrikse	Delft University of Technology
	Ir. T. Willems	Siemens Gamesa Renewable Energy
Thesis committee:	Prof. dr. P.G. Steeneken	Delft University of Technology
	Dr. ir. H. Hendrikse	Delft University of Technology
	Ir. T. Willems	Siemens Gamesa Renewable Energy
	Dr. ir. J.F.L. Goosen	Delft University of Technology


TU Delft
Delft
University of
Technology


SIEMENS Gamesa
RENEWABLE ENERGY

Abstract

The offshore wind industry is a relatively new but fast growing field in the global shift towards renewable energy to reduce carbon emissions. However, more difficulties arise in the design of an offshore wind turbine (OWT) compared to an onshore wind turbine, as the offshore structures are exposed to more environmental influences. One of those is sea ice. As wind farms are being built in areas where floating sea ice exists, such as the Baltic Sea and Bohai Bay, the effect of interaction of ice with an offshore wind turbine needs to be taken into account in the design phase. Several accidents have taken place in the past, where offshore structures such as bridges, lighthouses and oil platforms were exposed to severe ice loading, leading to human discomfort and damage or even failure of the structure. Recent research has shown that ice-induced vibrations (IIV) can develop in wind turbines with a monopile foundation. This research studies IIV in a wind turbine with a jacket foundation, which is used in deeper waters.

These IIV can be categorized into three regimes: intermittent crushing (IC), frequency lock-in (FLI) and continuous brittle crushing (CBR), depending on both structural and ice properties. During IC, which occurs for low ice velocities, large forces act on the structure. For higher velocities, the failure of ice 'locks in' with one of the structural eigenmodes, leading to the FLI mode, where cyclic loading of the structure sustains. This periodic movement affects the fatigue of the structure. When ice is moving at even higher velocities, the CBR regime begins, in which the ice load does not show a periodicity but fluctuates around a relatively low mean value, resulting in small, random oscillations of the structure around the mean deflection.

In this research, the effect of these IIV on offshore wind turbines with a jacket foundation was investigated. To that end, a structural model for a 5 MW wind turbine has been implemented and a preliminary study indicated that the second eigenmode is most susceptible to FLI. Next, the structural model has been coupled to a phenomenological ice model which simulates the three regimes of IIV. Case studies have shown that all IIV regimes do occur in the OWT when ice is acting on the structure; large displacements of the structure occur in IC and sustained oscillations take place in the second bending mode during FLI. Moreover, it was shown that the angle of incidence of ice has no effect on the IIV due to symmetry in the model. On the other hand, the chosen damping values have a large influence on the occurrence of IIV. Finally, it was found that a wind force solely can increase the displacements during IIV, but the aerodynamic damping involved reduces them.

Table of Contents

List of Figures

Glossary

List of Acronyms

CBR	continuous brittle crushing
FLI	frequency lock-in
FRF	frequency response function
GRE	global relative error
IC	intermittent crushing
IEC	International Electrotechnical Commission
IIV	ice-induced vibrations
ISO	International Organization for Standardization
OC4	Offshore Code Comparison Collaboration Continuation
OWT	offshore wind turbine
RNA	rotor and nacelle assembly

Acknowledgments

Now I am writing the last part of this thesis, my time as a student has almost come to an end. A good moment to express my gratitude to all of you who supported me during this journey.

First of all, I am grateful for the support from my supervisors. Tom, thank you for all the constructive discussions and brainstorms during the weekly meetings. Besides, you were always there to help when I came to your desk when I was stuck. Hayo, many thanks for all knowledge sharing and insights. Your enthusiasm for the topic is infectious, I always left your office with a good feeling. And Peter, thank you for the all the helpful meetings, in which you always kept the thesis goal and fundamentals in mind.

Thanks to all Siemens Gamesa colleagues and fellow students for the fruitful discussions, but also for distracting my mind during table football, beach volleyball, squash, coffees and drinks. The open and warm atmosphere in the department made my time in the office very pleasant.

Besides the support from TU Delft and the company, I would like to express my gratitude to my friends and family for the mental support you provided. Henri, thank you for always being there for me and for all the love and patience you had. Last but not least, I am very grateful for the endless support of my mum, dad and brother during my entire studies, you are the best!

Den Haag, November 20, 2018 Irene Marsman

Chapter 1

Introduction

In the fight against climate change, the European Union has set itself the binding target to gain 20 % of the power consumed in Europe from renewable resources in 2020. Moreover, a recent update of these goals stipulates that 27 % of the energy should be generated from renewable sources in 2030 (Newell, 2018). As reported by WindEurope (2018), wind energy currently provides more than 11 % of the European energy demand and is the most competitive and fastest growing renewable energy source.

1-1 Offshore wind turbines

In order to compete with fossil fuels and to make wind energy even more attractive, ongoing developments are aimed at further reducing the cost of wind energy production. Therefore the capacity per turbine is increasing, leading to larger structures. Due to constraints on turbine size, a lack of land availability and for reasons of visual impact and noise, offshore wind energy is getting more attention (Bilgili et al., 2011). According to WindEurope (2017), one quarter of the total wind energy production in 2020 will be from offshore.

In shallow waters up to approximately 35 meters, wind turbines are built with a monopile foundation (Figure 1-1a). However, offshore wind farms will gradually move further away from the coast, where the wind conditions are more favorable; wind speeds are higher and the flow is more uniform (Colmenar-Santos et al., 2016). In addition to higher wind loads, the wave conditions are more severe at these locations, and a more solid support structure is required to cope with these loads. Here, jacket foundations (Figure 1-1b) are economically more feasible to use at larger depths, since less material is needed to obtain the desired structural properties compared to a monopile foundation (Voormeeren et al., 2014).

Besides the wind and wave loads, ice loads have to be taken into account when designing an offshore wind turbine for locations where floating sea or lake ice exists. For example, in every winter sea ice grows in the Baltic Sea, Gulf of Bothnia and Bohai Bay, where wind turbines are planned and constructed. From the 1960s, ice-induced vibrations (IIV) are observed in structures such as lighthouses, bridges and oil and drilling platforms (Yue et al., 2009). These

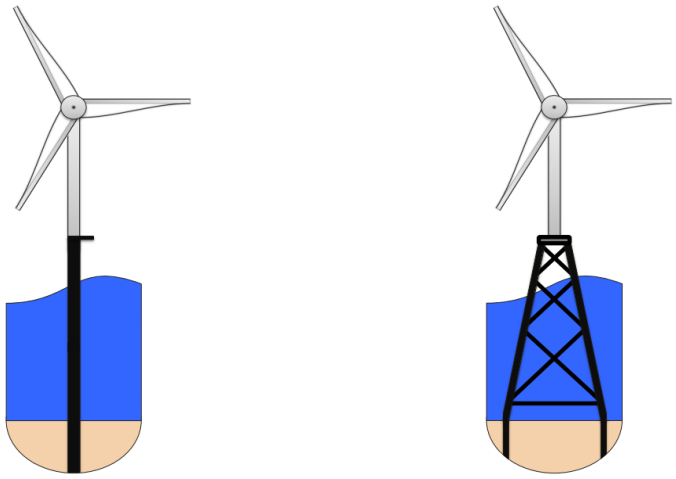

(a) Monopile **(b)** Jacket

Figure 1-1: Two foundation types that are commonly used for offshore wind turbines (Van der Valk, 2014).

IIV can cause high peak loads and severe oscillations (Hendrikse et al., 2014), resulting in damage to or even failure of the structures. Ice loads can therefore be the dominant loads on offshore structures in ice-infested areas (Sanderson, 1988; Liu et al., 2009b) and need to be considered in the design of offshore wind turbines.

1-2 Ice model applied to wind turbine on monopile foundation

Since the encounter of IIV, several ice models have been developed. The difficulty of ice modeling lies in the fact that the ice force is a (nonlinear) function of the structural displacement and vice versa, and therefore a coupled model is needed. Recently, the model as proposed and validated by Hendrikse and Metrikine (2016) is applied to a wind turbine on a monopile foundation in the research by Willems (2016). Ice-induced vibrations are shown to occur for the case where only ice loading is applied. The study revealed that modeling both wind and ice loads simultaneously leads to lower damage than the ice-only case, which is attributed to aerodynamic damping.

1-3 Research on ice-induced vibrations of jacket structures

To the author's knowledge, research on ice-induced vibrations of jacket structures is only done to jacket structures constructed with cones on the legs at sea level (Wang et al., 2013, 2016; Liu et al., 2009a). The inclined angle of the cones bends the ice sheet out-of-plane, making it fail in bending instead of crushing. This mechanism reduces the ice force (Liu et al., 2009a; ISO 19906, 2010). The drawbacks of ice cones are that they are costly and increase the wave loads due to the additional area. It is therefore desired to avoid the use of these ice breaking cones. However, to safely build a jacket foundation without these cones, the effect of ice on the structure need to be known.

1-4 Thesis objective and outline

In this thesis, the research on ice-induced vibrations of wind turbines with a monopile foundation (Willems, 2016) is extended to turbines with a jacket foundation. The objective of this thesis is to *model the dynamic interaction between an ice sheet and an offshore wind turbine with a jacket foundation and identify the resulting effects*. This facilitates the design of an offshore wind turbine which can resist loading caused by floating ice sheets.

First, the IIV are explained in Chapter 2 and several models simulating them are given. Then, a structural model of a wind turbine on a jacket foundation is constructed to which the ice loading can be applied, which is described in Chapter 3. Thereafter, the chosen phenomenological model (by Hendrikse et al. (2018)), which simulates the forces exerted by ice, is studied and implemented numerically, as explained in Chapter 4. Thereafter, the two models are coupled to obtain a tool for performing fully integrated simulations of sea ice interacting with a wind turbine on a jacket foundation. This coupling is described in detail in Chapter 5. The studied load cases and the tools for post-processing are given in Chapter 6 and 7, respectively.

Finally, using the coupled model, simulations with varying ice speeds, ice thicknesses and angles of approach are performed to draw a conclusion on the effects and occurrence of ice-induced vibrations. In addition, simulations are done to test the effect of the implementation of damping and the effect of wind force on IIV. All results are presented in Chapter 8. The findings are concluded in Chapter 9, where also recommendations for future developments are given.

Chapter 2

Sea ice mechanics

The failure modes of ice sheets are explained in this chapter. Due to the flexible nature of vertically sided structures, several ice-induced vibrations (IIV) can occur during the interaction with ice, which can cause high loads and severe damage. Therefore, the effect of interaction between sea ice and offshore structures needs to be considered in the design. These IIV are described and models simulating its dynamics are explained, with special attention to the one that is used in this study.

2-1 Failure modes

In order to determine the failure modes of ice, based solely on its properties, the response of ice acting on a horizontal rigid body is studied first by doing laboratory tests (Hendrikse, 2017). It was found that ice fails in a brittle or ductile manner, depending on the compressive strain rate, as depicted in Figure 2-1. As the structure is rigid, the compressive strain ($\dot{\varepsilon}$) rate is determined by the ice velocity (v_{ice}) only.

Next, the effect of the aspect ratio of the structure (defined by structure width d divided by ice thickness h) on the failure mode is studied and a failure map as in Figure 2-2 is created. Three main failure modes are distinguished: creep, crushing and buckling. They are explained next.

At low velocities and low aspect ratios, the ice fails in a ductile manner and creeps around the structure, resulting in full contact and a uniform pressure distribution at the interface. As a result, the forces on the structure can become very high (Hendrikse, 2017). For increasing velocities within this ductile regime, the maximum compressive stress increases with increasing velocity, as can be seen in Figure 2-1. This phenomenon is called strain rate hardening (Schulson and Duval, 2009).

For higher ice velocities and low aspect ratios, the ice fails by crushing. Ductile dislocations in the ice do not have time to develop and the ice pulverizes directly in front of the structure, forming small pieces of ice rubble. Consequently, the contact area is irregular and coarse,

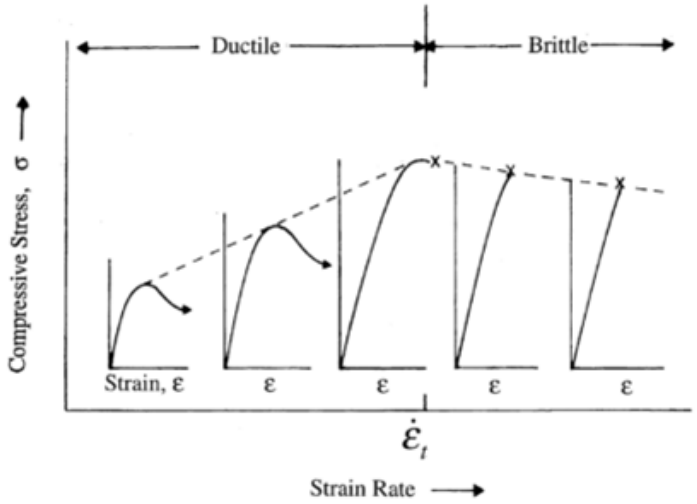

Figure 2-1: Schematic stress-strain curves for compression of ice. It behaves ductile at low strain rates and brittle at higher strain rates. Graph from (Schulson and Duval, 2009).

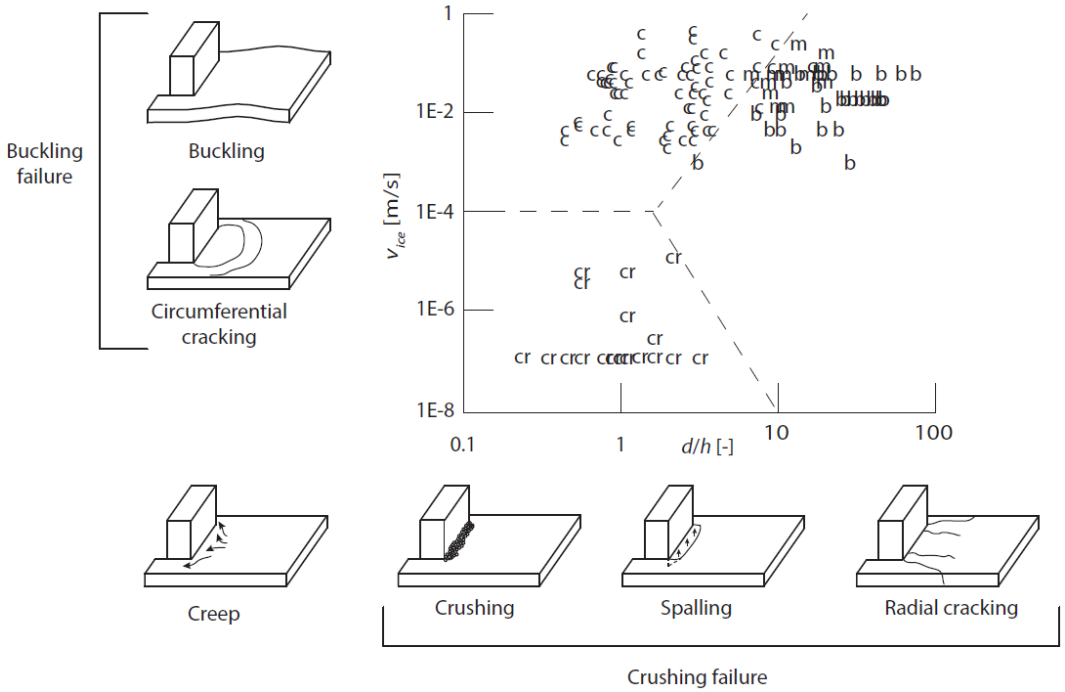

Figure 2-2: Failure modes and failure map by Hendrikse (2017) based on Timco (1991). The following abbreviations for failure mechanisms are used: cr (creep), c (crushing), b (bucking) and m (mixed crushing and buckling).

resulting in lower net forces acting on the structure for these higher ice velocities (Sodhi and Haehnel, 2003). Spalling (or flaking) and formation of radial cracks occur in the same regime of velocities as the crushing described above. Spalling is characterized by cracking from the vertical interaction area to the lower or upper surface of the ice, after which these fragments are cleaved from the surface, having a half-circular or triangular shape (Blanchet et al., 1988). As a result, a line-like contact area around the midsection remains (Takeuchi et al., 2001). This failure mode only arises for low aspect ratios ($d/h < 3$). The formation of radial cracks, originating from the structure, occurs for wider structures (Schulson and Duval, 2009).

For all ice velocities, but only at relatively high aspect ratios, the ice can buckle out-of-plane, as displayed schematically in Figure 2-2. When failing in this mode, circumferential cracks form at the location where the flexural strength is exceeded (Willems, 2016).

Splitting and bending are not taken into account in this research. As these failure modes release the load acting on the structure, the result will be an over-estimation, and thus conservative when neglecting the effects.

2-2 Ice-induced vibrations

Due to the compliance of a flexible structure, the relative velocity between the ice and structure at sea level varies in time, contrary to the interaction with a rigid indenter. As a result, the failure modes alternate, giving rise to IIV (Sodhi and Haehnel, 2003). Three regimes of IIV (also denoted as crushing regimes) are distinguished: intermittent crushing (IC), frequency lock-in (FLI) and continuous brittle crushing (CBR), as illustrated in Figure 2-3. Time series of the structural displacement in the three regimes are given in Figure 2-4. Using these graphs, the crushing regimes are explained next.

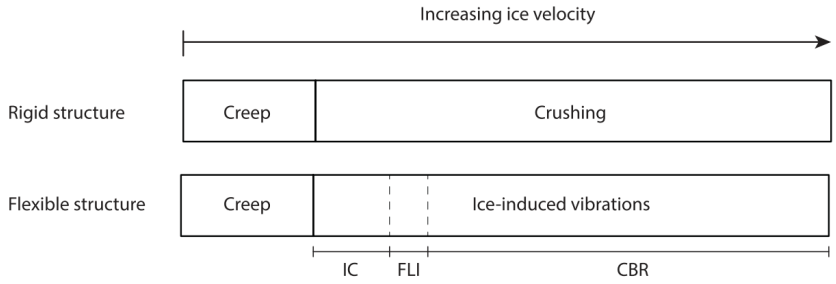

Figure 2-3: Schematic representation of crushing regimes. When ice interacts with a rigid structure, a distinction can be made between creep and crushing. When the structure is flexible, the crushing regime consists of three parts: intermittent crushing, frequency lock-in and continuous brittle crushing. The dashed lines indicate the transition velocity between the regimes. Image from Hendrikse (2017).

2-2-1 Intermittent crushing (IC)

Intermittent crushing occurs when an ice sheet hits the structure relatively slowly. During loading, the structure deflects in the direction of ice motion, decreasing the relative velocity. This results in ductile failure and a gradual increase of the contact area and ice force. When

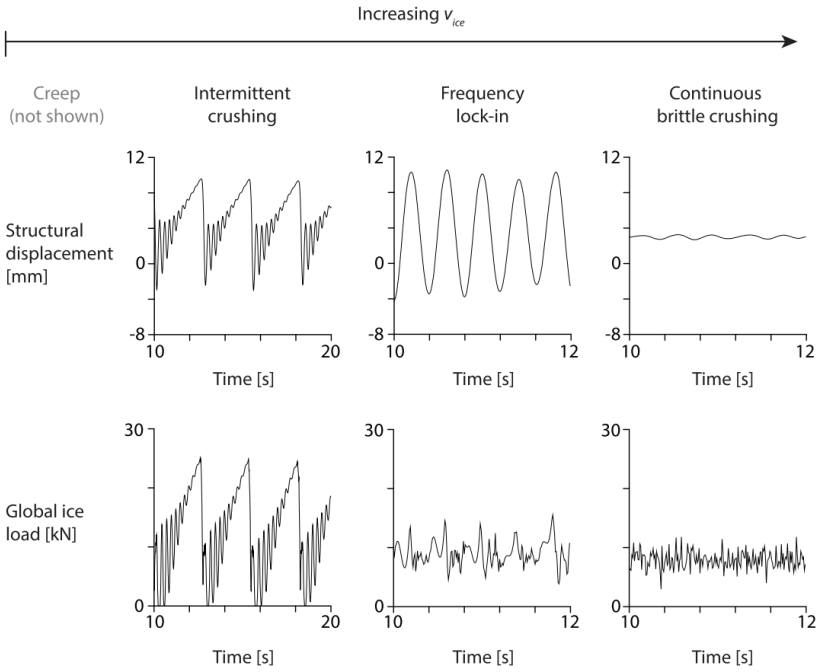

Figure 2-4: Three ice-induced vibration regimes as function of ice velocity (Hendrikse, 2017). The structural displacement is shown in the first row and the ice load in the second.

the point of maximum deflection is reached, the strain energy stored in the structure is released and the ice sheet starts to fail, resulting in a high structural velocity opposite to the ice motion. During this unloading phase, the ice fails in a brittle manner, which results in a load drop as seen in the lower left graph of Figure 2-4. The structure possibly vibrates around its equilibrium position, depending on the ice velocity. When a certain decay of the oscillations is reached, the relative velocity is low enough to start a new loading cycle (Sodhi and Haehnel, 2003), generating a sawtooth-like pattern for the force and displacement.

2-2-2 Frequency lock-in (FLI)

The frequency lock-in regime can be invoked in a range of intermediate ice velocities. Analogous to intermittent crushing, both ductile loading and brittle unloading phases are distinguished. As seen in the second column of Figure 2-4, the timing of ductile loading synchronizes, or 'locks in', with the sinusoidal displacement of the structure, close to one of the lower eigenfrequencies of the structure (Hendrikse, 2017). When the damping is low, the structural displacements will be large, and due to the large amount of repetitions in this failure mode, frequency lock-in can cause fatigue in the structure (Willems, 2016). According to the International Organization for Standardization (ISO) (ISO 19906, 2010), structures which have fundamental frequencies in the range of 0.4 Hz to 10 Hz are susceptible to frequency lock-in, when they have a structural damping lower than 3 % critical, for ice velocities up to $0.1\,\mathrm{m\,s^{-1}}$. Kärnä et al. (2013) state that FLI is observed for ice velocities up to $0.15\,\mathrm{m\,s^{-1}}$.

2-2-3 Continuous brittle crushing (CBR)

At high ice velocities, the ice crushes continuously. The relative velocity between the ice and structure remains high and the ice does not have time to deform in a ductile manner. The resulting force on the structure is relatively low and fluctuates randomly around a mean value, similar to the crushing behavior against a rigid structure. The structural displacement therefore randomly fluctuates around a constant displacement value. The effect due to CBR is insignificant compared to the intermittent crushing and frequency lock-in regimes.

2-3 Ice modeling

As the phenomena involved in ice-structure interaction are very complex, approximations of forces due to floating sea ice are made. Phenomenological models are developed which describe the ice behavior, based on measurements and laws in for example viscoelastic theory. They are used to simulate the ice-structure interaction and predict the occurrence of IIV. However, the models do not explain the underlying and detailed physics and several assumptions are made. Properties such as temperature, density, salinity, brine volume and grain size determine the strength and other properties of the ice (Weeks, 2010). They can differ per ice floe and internal location, but are considered constant. That also indicates that ice features, like ice bergs and ridges, are not incorporated in the models, as well as the effect of broken ice rubble.

The first part of this section describes the approach by two technical standards organizations. The second part explains the three main categories of phenomenological models, where the latter is used in the research.

2-3-1 Standards

The two design standards discussed in this section, from the International Organization for Standardization (ISO) and the International Electrotechnical Commission (IEC), have in common that an ice load time series is created in advance and applied to the structure. In this way, the interaction between structure and ice is neglected and the occurrence of ice-induced vibrations is preset instead of predicted.

International Organization for Standardization

In the ISO standard containing requirements and assessments for offshore structures in the petroleum and natural gas industry, load time series are given for the intermittent crushing and frequency lock-in regimes (ISO 19906, 2010), as depicted in Figures 2-5 and 2-6 respectively.

For intermittent crushing, the period of ice action T is larger than the period of the first structural eigenmode. In addition, during part of the period of ice action, the ice force on the structure can be zero when there is no contact.

For frequency lock-in, the period of ice action is set equal to one of the natural frequencies, which all need to be checked below 10 Hz. The peak values $F_{\max}$ are assumed to be constant and determined by:

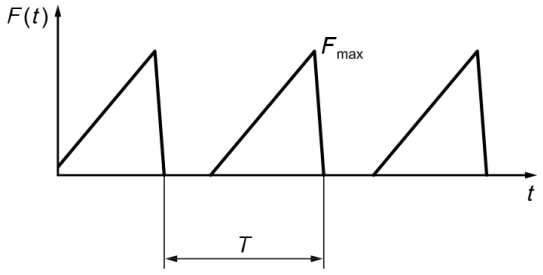

(a) Period of the ice action (T) is larger than the duration of the force applied.

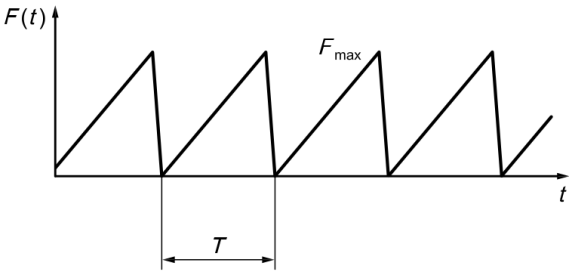

(b) Period of the ice action (T) is equal to the duration of the force applied.

Figure 2-5: Time load series for intermittent crushing as given in ISO 19906 (2010).

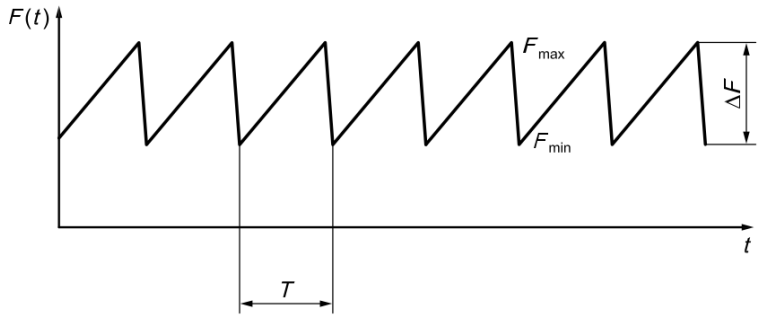

Figure 2-6: Time load series for frequency lock-in as given in ISO 19906 (2010).

$$F_{\max} = F_{\mathrm{G}} = p_{\mathrm{G}} h w = C_{\mathrm{R}} \left(\frac{h}{h_1}\right)^{-0.50+h/5} \left(\frac{w}{h}\right)^{-0.16} h w, \tag{2-1}$$

where p_{G} is the average ice pressure in pascal, w the projected width of the structure in meters, h the thickness of the ice sheet in meters and h_1 a reference ice thickness of 1 meter. C_{R} is the ice strength coefficient in pascal, which can have a value up to 2.8 MPa in full scale ice events and up to 5 MPa in laboratory tests (Palmer and Croasdale, 2013), based on measurements. p_{G} is the global ice pressure averaged over the nominal contact area wh. Equation 2-1 holds for cases where the ice sheet thickness h is less than 1 meter and in which the aspect ratio w/h is larger than 2.

International Electrotechnical Commission

In the standard for offshore wind turbines by the International Electrotechnical Commission (IEC), the maximum static horizontal load H_{d} (in newton) from moving ice due to crushing is calculated as

$$H_{\mathrm{d}} = k_1 k_2 k_3 h D \sigma_{\mathrm{c}}, \tag{2-2}$$

based on the findings of Korzhavin (1962). Here, k_1, k_2 and k_3 are the dimensionless structure shape factor, contact factor and aspect ratio factor, respectively. The crushing strength (σ_{c}) has a value between 1.5 MPa and 3.0 MPa, depending on the temperature and ice floe velocity. h is the ice thickness and D the diameter of the support structure at water line, both in meters.

This maximum static horizontal load is used in the dynamic load simulation if data is not available. The variation of loading on vertical structures is approximated by (Shi et al., 2016):

$$H_{\text{dynv}} = H_{\text{d}} \left(\frac{3}{4} + \frac{1}{4} \sin\left(2\pi f_{\text{N}} t\right) \right), \tag{2-3}$$

where t is the time in seconds and f_{N} an eigenfrequency of the structure in hertz. The first two eigenfrequencies should be checked, according to the standard. For a more detailed explanation of the loads, the reader is referred to the standard documentation (IEC 61400-3:2009, 2009).

2-3-2 Ice models

Since the physics that govern ice-induced vibrations is not fully understood, several researchers tried to develop phenomenological models that accurately simulate and predict ice-structure interaction, based on laboratory and full-scale measurements. Ice-structure interaction was first reported by Peyton (1968), who did measurements on oil platforms and single vertical piles at Cook Inlet, Alaska. Based on his findings, several phenomenological models have been proposed which can roughly be divided into two categories: models based on a fixed failure length and models based on self-excited vibration (Muhonen, 1996). These two theories were developed in the sixties and seventies and are still used. However, they are being debated in the community on ice mechanics (Huang et al., 2007), with arguments that are discussed later. More recently, models based on the variation of contact area arose. A model based on this idea (Hendrikse and Metrikine, 2015) is used in this thesis. All three categories are explained next.

Failure length

This first category of ice models is based on a fixed failure length of crushing ice, resulting in a fixed frequency of ice failure for a given ice velocity. The development of ice-induced vibrations is then explained as either a result of a periodic load or a synchronization of the structural natural frequency with the failure frequency of the ice (Peyton, 1968; Huang et al., 2007; Hendrikse, 2017). The first who developed a model based on a failure length are Matlock et al. (1969). In this model, the ice is represented as a series of elastic-brittle cantilevers on a roller supported rigid base, as shown in Figure 2-7a. When the front cantilever (cantilever 1) comes into contact with the structure, it will deform by δ, as a function of the relative displacement. As a result, a proportional force Q acts on the system. If the maximum deflection δ_{max} is reached, the cantilever breaks and is removed. The load then drops to zero until the next cantilever comes in contact, resulting in the sawtooth pattern as shown in Figure 2-7b. The approach proposed by ISO 19906 (2010) is a simplification of this model, since the sawtooth wave output force is used as an input to a structure. Other models based on a failure length are Eranti (1992), Sodhi (1995) and Withalm and Hoffmann (2010) for example.

Debaters in literature, for example Blenkarn (1970), Hendrikse and Metrikine (2015) and Ji and Oterkus (2017), argue that the resulting failure frequency should also be visible in field data of fast moving ice acting on a rigid structure and failing in the brittle regime, but such frequencies are not observed.

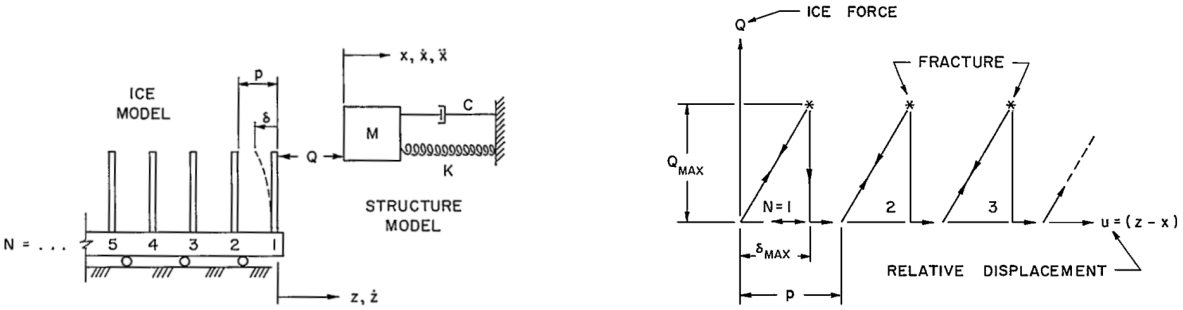

(a) Schematic of Matlock's model, where cantilevers are mounted on a roller supported rigid base.

(b) Resulting ice force on the interacting structure.

Figure 2-7: Ice model by Matlock et al. (1969).

Self-excited vibration

Another explanation for ice-induced vibrations, such as in the models of Blenkarn (1970) and Määttänen (1978), lies in a negative gradient in the failure stress as a function of strain rate, the so-called negative damping, as depicted in Figure 2-8. Blenkarn explains that for increasing loading rates at the right side of the peak, the force acting on the structure is decreasing, resulting in a decrease of structural velocity and therefore a decrease in loading rate: self-excited vibration. He states that the load will increase until the ice strength is reached.

However, a negative gradient in the stress-strain curve like in Figure 2-8 is not always observed in measurements on warm ice, while ice-induced vibrations mainly occur during warmer periods (Hendrikse, 2017). In the models based on the idea of a negative damping, parameters need to be adjusted for different structures, implying that the ice behavior is dependent on the geometry of the structure. Clearly, the models do not fully capture the physics of ice-structure interaction.

Some models contain concepts of both theories, such as the model by Huang and Liu (2009) and Kärnä and Turunen (1989), but are not discussed here.

Non-simultaneous failure

The third class of models is slightly newer than the previous two. P.R. Kry is cited in many researches to be the one who developed the concept of non-simultaneous failure in 1978 (actual paper not found). He divided the contact area between ice and structure in narrow independent zones at which the ice fails non-simultaneously (Eranti, 1992), due to the irregularity of the ice surface, as sketched in Figure 2-9. Then, to obtain the total force acting on the structure, the forces at the contact zones are summed, resulting in the global ice force. Based on this idea, several ice models were proposed, such as Ashby et al. (1986), Sanderson (1988), Eranti (1992) and Daley (1992).

The phenomenological model that is used in this research is also based on this principle. Hendrikse and Metrikine (2015) proposed a model based on forced vibration measurements on ice interacting with a rigid structure, performed at a large ice basin at HSVA, Hamburg.

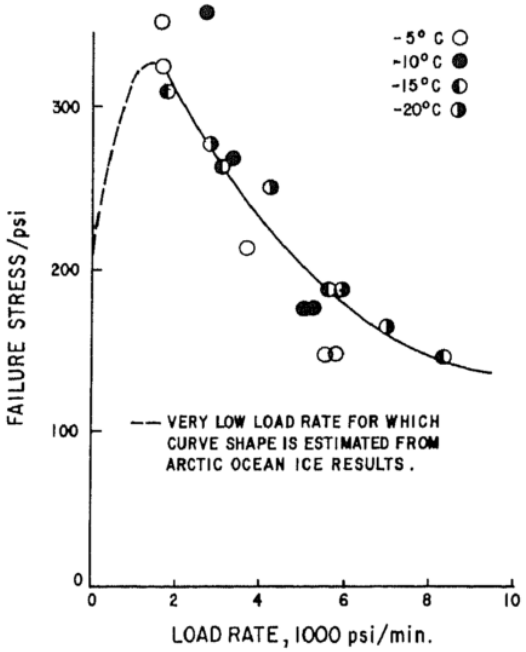

Figure 2-8: Relation between compressive failure stress as a function of strain rate. The negative gradient is often referred to as negative damping and is used in several ice models as a source of ice-induced vibrations. Graph from Peyton (1968).

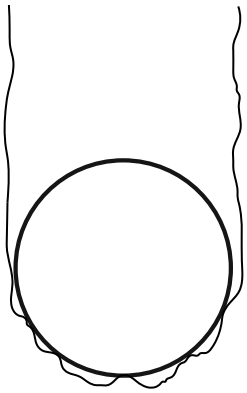

Figure 2-9: Schematic of irregular contact area between ice and structure (top view).

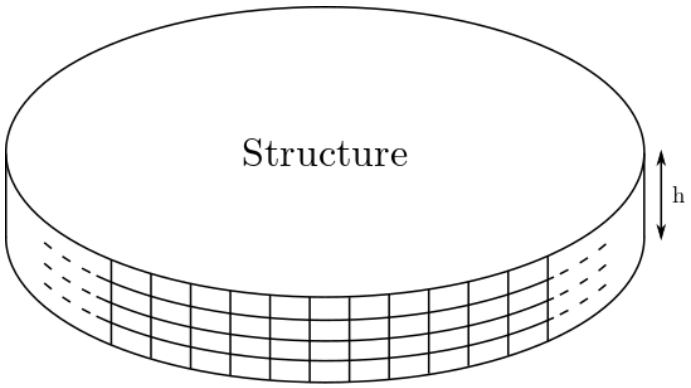

Figure 2-10: The force at the interaction area between ice and structure is measured using tactile sensors placed at the interface. The height of the interaction area is equal to the ice thickness h.

The pressure of ice acting on a structure was measured using tactile sensors on the interface between the two, as illustrated in Figure 2-10. For a comprehensive description of the experiment and the results, the reader is referred to Hendrikse (2017).

To demonstrate the phenomenon, a time series of the ice load and contact area in the intermittent crushing regime is used, shown in Figure 2-11, where the measured contact pressures are plotted for time moments A, B and C in Figure 2-11c.

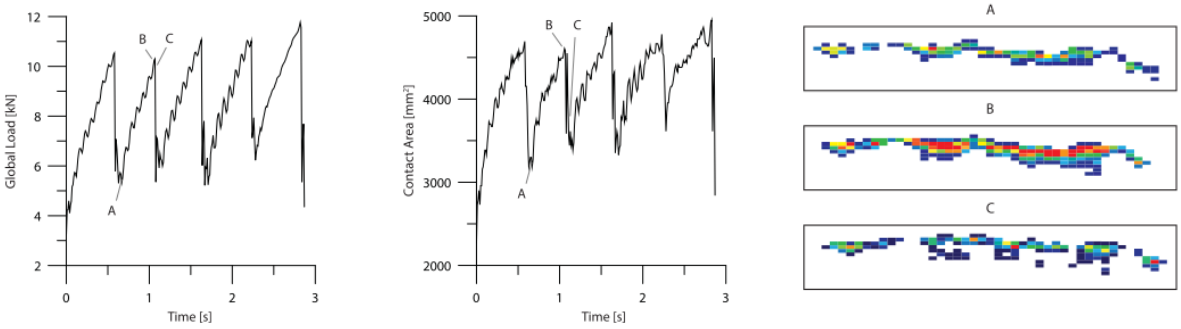

(a) Global load during intermittent crushing, similar to the graph in Figure 2-4.

(b) Graph of the contact area during intermittent crushing.

(c) Local contact zones at three moments in the intermittent crushing cycle. Red indicates a high pressure and blue a low pressure.

Figure 2-11: Global load, contact area and local pressures during intermittent crushing failure with a constant ice velocity of 40 mm s^{-1} (Hendrikse, 2017). It can be seen that the contact area and total load on the structure increase from start (point A) towards maximum deflection (point B). After the maximum is reached, local brittle failure occurs and the structure moves back through the ice. During this process, the load is low and the contact area is small (point C).

At moment A, an intermittent crushing cycle starts. The relative velocity between ice and structure is low, which allows for ductile deformation to develop, increasing the contact area and therefore the pressure acting on the structure. The structure deforms until moment B, when the maximum compressive force is reached. Local parts of the ice, where the maximum deformation is reached, start to break, thereby increasing the load on the remaining parts. This initiates a chain of brittle failure, during which the load drops drastically to moment C, where the contact area is small. The structure moves back through the ice and a new cycle starts when the structure is slowed down.

The model of Hendrikse and Metrikine (2015) defines local contact zones, each interacting with an individual ice element. The model was later adjusted; the latest version, as proposed in Hendrikse et al. (2018), is used in this research and is explained in Chapter 4.

Chapter 3

Offshore wind turbine model

This chapter discusses the offshore wind turbine and its numerical model. The main components of an offshore wind turbine are shown in Figure 3-1. During operation, the wind sets the blades of the rotor in motion, which is connected to the main shaft through the hub. In the nacelle, the mechanical energy of the shaft is converted into electrical power by a generator. These top parts together are referred to as the rotor and nacelle assembly (RNA). The tower and foundation, connected by the transition piece, form the support structure of the offshore wind turbine. In the next section, the numerical implementation is discussed per part in more detail.

To study the behavior of the structure as a result of ice forces, a reference model for an offshore wind turbine is used and implemented in MATLAB, which is depicted in Figures 3-2 and 3-3. The jacket was originally designed in the UpWind project and further developed in the Offshore Code Comparison Collaboration Continuation (OC4) project, to be used for code-to-code comparison. The support structure is designed for a 5 MW turbine in waters of 50 m deep, as described by Jonkman et al. (2009). A detailed description of the complete jacket model can be found in Vorpahl et al. (2013), a short summary is given here.

3-1 Jacket foundation

The jacket foundation consists of four legs linked by four levels of cross braces. All beam elements are tubular and are modeled with Timoshenko beam theory. The beam formulation and assembly process are described in detail by Géradin and Rixen (2015). The connection to the seabed is considered rigid and thus the six degrees of freedom at the bottom are fixed, ignoring any soil-structure interaction, which results in higher eigenfrequencies of the structure. Marine growth on the structure and flooding of the legs is accounted for by lumping the distributed masses to the nodes below sea level, resulting in lower eigenfrequencies.

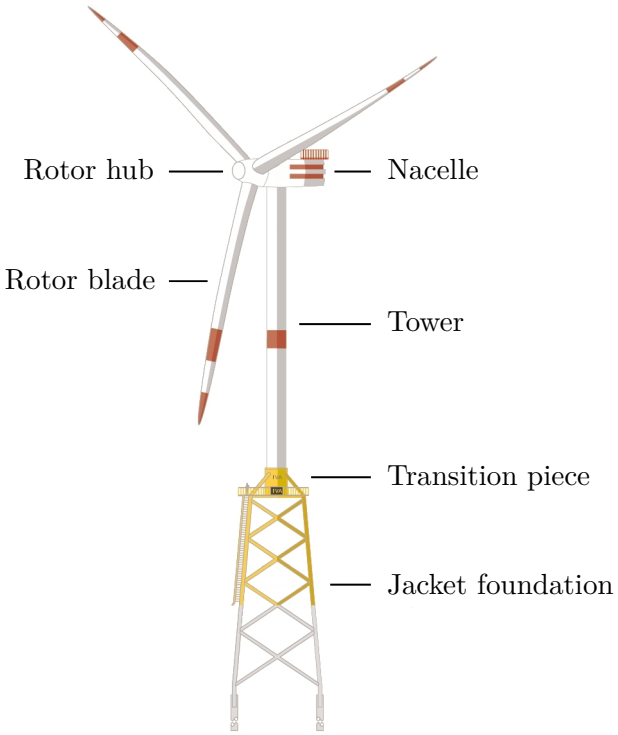

Figure 3-1: Components of an offshore wind turbine (BINE Information Service).

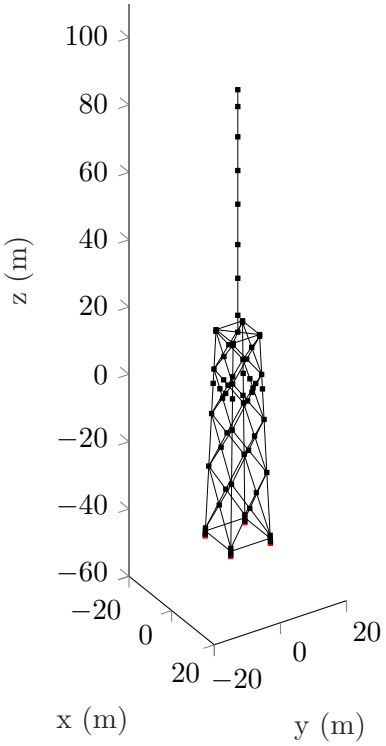

Figure 3-2: The structural model in MATLAB, extra nodes are added at mean sea level.

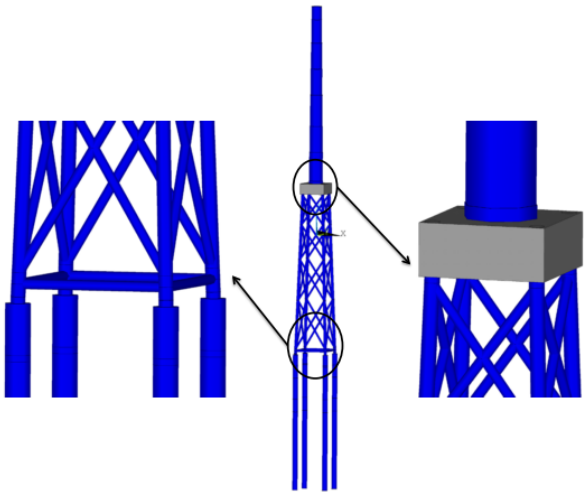

Figure 3-3: The OC4 jacket model as described in Vorpahl et al. (2013). The long foundation piles are modeled as a rigid connection to the seabed. The tower consists of several tubular sections. On top of the tower, the RNA is modeled by a point mass.

3-2 Transition piece, tower and RNA

On top of the jacket, the transition piece (a heavy concrete block) is modeled. This is done by adding a stiffness between the four top corners, which has a value of 25 times the value of the stiffest beam in the model. This value is chosen such that the differences between stiffnesses do not become too large while retrieving the correct eigenvalues of the structure. The mass of the concrete block is divided over the four corners as point masses.

The conical tower is represented by eight tubular beam sections of decreasing diameter towards the top. The RNA is modeled by a point mass at the upper node.

3-3 Equations of motion

Assembly of the beam elements and point masses yields the following system of N_s equations of motion:

$$\mathbf{M}\ddot{\mathbf{x}}(t) + \mathbf{C}\dot{\mathbf{x}}(t) + \mathbf{K}\mathbf{x}(t) = \mathbf{f}(t), \tag{3-1}$$

where $\mathbf{M}$ is the mass matrix, $\mathbf{C}$ the damping matrix and $\mathbf{K}$ the stiffness matrix. Solving the equations yields the N_s nodal displacements $\mathbf{x}$ due to force $\mathbf{f}$. Vorpahl et al. (2013) define the damping of the structure as 0.01, or 1 % critical, for all modes of the support structure. This damping model is referred to as modal damping. However, in this study, the damping is defined as the damping of the complete turbine.

However, finding the structural damping is difficult (Damgaard et al., 2013; Devriendt et al., 2013) and is mostly done to only the first natural frequency. Therefore, the trend of higher structural damping values is unknown. Therefore, another form of damping is considered in this research: Rayleigh damping (or viscous damping). The Rayleigh damping matrix is a linear combination of the mass and stiffness matrix:

$$\mathbf{C} = \alpha\mathbf{M} + \beta\mathbf{K}, \tag{3-2}$$

where α and β are constants of proportionality. They are found by setting the modal damping ratio ζ of the first two distinct undamped eigenmodes to 0.01, or 1 % critical. The damping of the higher modes is then higher and follows a trend as determined by α and β. The modal damping matrix is constructed by setting all modal damping ratios to 0.01, as explained further in Section 5-2. The resulting damping values for the two models as a function of eigenfrequency are plotted in Figure 3-4. From now, these two types of damping are referred to as 'Rayleigh damping model' and 'modal damping model'.

3-4 Eigenfrequencies and eigenmodes

After assembly of the structural model and deriving its mass and stiffness matrices, the undamped eigenmodes can be obtained. The first six distinct eigenfrequencies and eigenmodes are given in Table 3-1 (symmetric eigenmodes have an equal eigenfrequency), a graphical representation is given in Figure 3-5. As the modes with an equal eigenfrequency have an identical eigenvector, but are perpendicular, the first and second mode together are from now

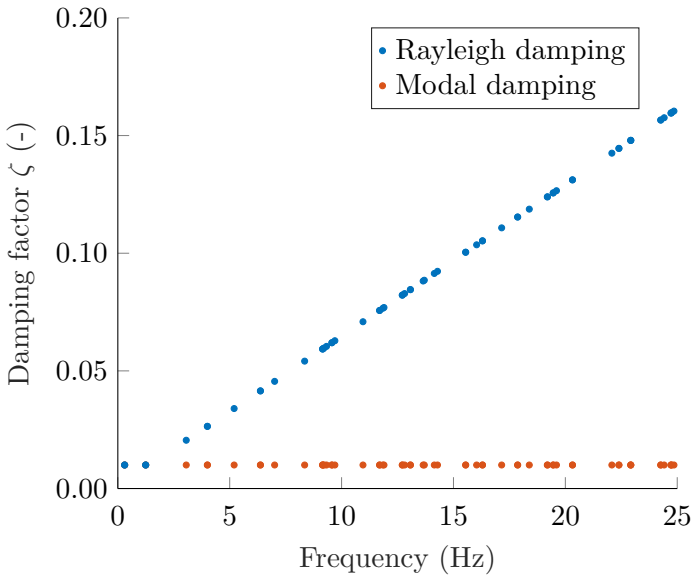

Figure 3-4: Damping values for each mode for the modal and Rayleigh damping cases.

on referred to as the first mode and the second and third mode together as the second mode. In total, the structural model contains 414 eigenmodes.

Table 3-1: First ten eigenmodes of the OC4 wind turbine.

Mode number	Frequency (Hz)	Description
1, 2	0.305	1^{st} bending mode
3, 4	1.245	2^{nd} bending mode
5	3.057	1^{st} torsional mode
6, 7	4.002	3^{rd} bending mode
8	5.198	1^{st} breathing mode
9, 10	6.373	4^{th} bending mode

3-5 Frequency response function

A preliminary estimation on the susceptibility of eigenmodes to frequency lock-in is obtained using a frequency response function (FRF). The modal amplitude FRF acts as a transfer function of a sinusoidal force F at degree of freedom p to the modal displacement u_i of mode i (Metrikine, 2017):

$$H_{u_i F_p}(\Omega) = \frac{\hat{u}_i}{\hat{F}_p} = \frac{1}{\sqrt{\left(1 - \left(\frac{\Omega}{\omega_i}\right)^2\right)^2 + \left(2\zeta_i \frac{\Omega}{\omega_i}\right)^2}} \frac{1}{\omega_i^2} \frac{\hat{x}_{pi}}{m_{ii}^*}, \tag{3-3}$$

where Ω is the frequency of the harmonic load applied. ω_i, ζ_i and m_{ii}^* are the modal frequency, damping ratio and mass, respectively.

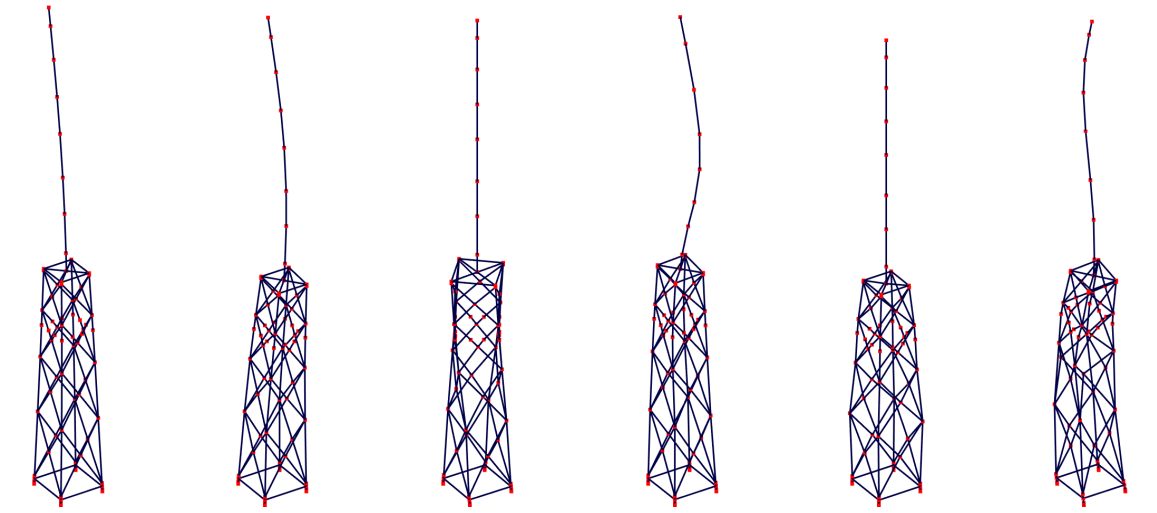

(a) Mode 1 0.305 Hz **(b)** Mode 3 1.245 Hz **(c)** Mode 5 3.057 Hz **(d)** Mode 6 4.002 Hz **(e)** Mode 8 5.198 Hz **(f)** Mode 9 6.373 Hz

Figure 3-5: The first six eigenmodes of the OC4 jacket, as described in Table 3-1.

The amplitude FRF, the transfer of a force at degree of freedom p to the displacement of degree of freedom x_q, yields:

$$H_{x_q F_p}(\Omega) = \frac{x_q}{\hat{F}_p} = \sqrt{\left(C_{qF_p}\right)^2 + \left(D_{qF_p}\right)^2}, \tag{3-4}$$

where

$$C_{qF_p} = \sum_{i=1}^{N_\mathrm{s}} \hat{x}_{qi} H_{u_i F_p}(\Omega) \sin\left(\varphi_i\right), \tag{3-5}$$

$$D_{qF_p} = \sum_{i=1}^{N_\mathrm{s}} \hat{x}_{qi} H_{u_i F_p}(\Omega) \cos\left(\varphi_i\right), \tag{3-6}$$

in which the summation runs over all N_s modes and where φ_i is the phase shift defined by:

$$\varphi_i = \arctan\left(\frac{2\zeta_i \frac{\Omega}{\omega_i}}{1 - \left(\frac{\Omega}{\omega_i}\right)^2}\right). \tag{3-7}$$

The response to forcing of the nodes at sea level are of main interest, since their displacement can invoke ice-induced vibrations. In Figure 3-6, the transfer function of three load cases to the displacement of node 44 in x-direction are plotted. As can be deduced from the graph, the second vibration mode has the highest transfer value for the in-phase loads (red and blue lines): a unit harmonic load causes the largest deflections of the loaded node. This is due to the large modal displacement of the second bending mode at the point of ice action. It is therefore expected that this mode is most susceptible to frequency lock-in (FLI). In the out-of-phase case (yellow line), mainly the rotation mode at 3.057 Hz is excited. However,

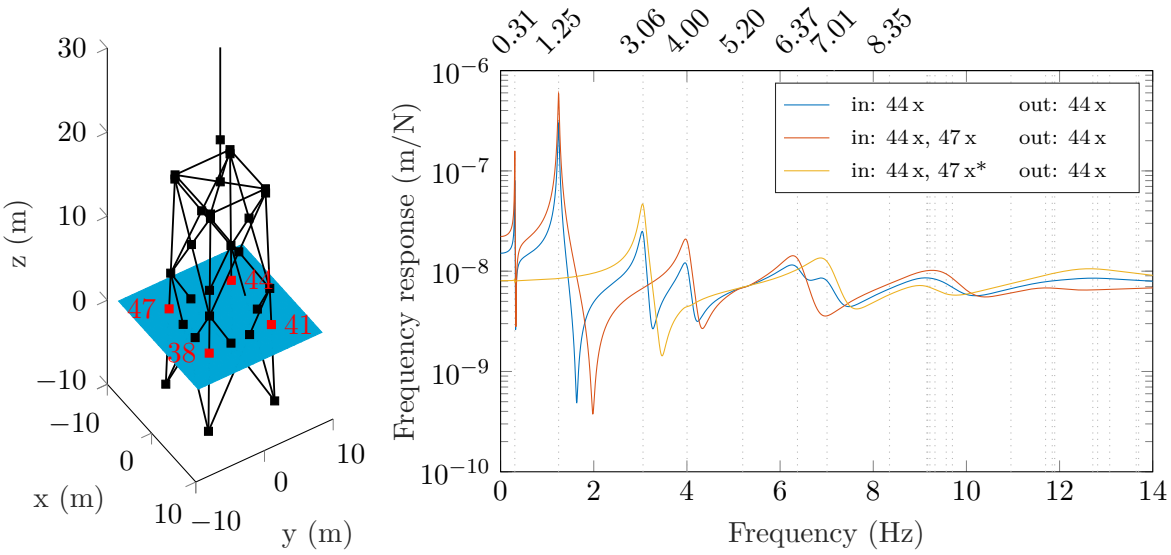

(a) Close up of jacket nodes at sea level.

(b) Frequency response functions, using the Rayleigh damping model.

Figure 3-6: The frequency response functions of node 44 in x-direction due to three different harmonic (sinusoidal) load cases: 1) node 44 is loaded in x-direction, 2) both nodes 44 and 47 are loaded in x-direction, in-phase, and 3) nodes 44 and 47 are loaded in x-direction, out-of-phase. The grey dashed lines indicate the eigenfrequencies with the values at the top axis for the modes below below 9 Hz. The asterisk indicates an out-of-phase loading. Rayleigh damping is used here.

the output displacement of this mode is less than both the first and second modes, so the occurrence of FLI in this mode is unlikely.

Chapter 4

Ice model

In this chapter, the phenomenological ice model proposed by Hendrikse and Metrikine (2015) (and later adjusted and verified by Hendrikse et al. (2018)) to simulate the ice-structure interaction is described in detail. First, the main idea of the model is explained in Section 4-1 and second, the kinematic elements that mimic the creep and crushing behavior are described in Section 4-2, where their equations of motion are given. This chapter is based on Hendrikse (2017) and Hendrikse et al. (2018). The numerical implementation is explained in the next chapter.

4-1 Kinematic elements

In order to simulate the contact area variation and its statistical properties, the ice at the interface with the structure is divided into N elements, as illustrated in Figure 4-1a. Each element consists of a combination of linear and non-linear springs and dashpots to simulate the creep and crushing of the ice, as shown in Figure 4-1b, where $x_{i,1}$, $x_{i,2}$ and $x_{i,3}$ are the displacements of the nodes in element i.

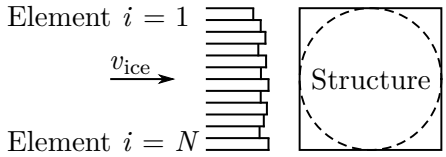

(a) Top view of the ice model interface. The interaction area is divided into N individual elements. The elements move towards the structure with ice velocity v_{ice}.

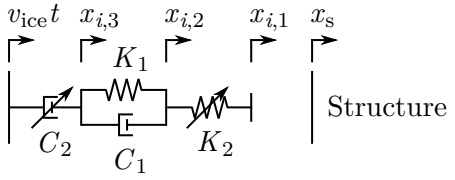

(b) Ice model element. It is similar to the Burgers model in rheological theory, consisting of a Kelvin-Voigt element (K_1 in parallel with C_1) in series with a Maxwell element (K_2 in series with C_2), but with a non-linear dashpot and spring.

Figure 4-1: Ice model by Hendrikse et al. (2018).

The nonlinear dashpot, C_2, represents the secondary creep in ice for very low loading velocities. The strain rate of the element is a function of the stress cubed, referred to as power law

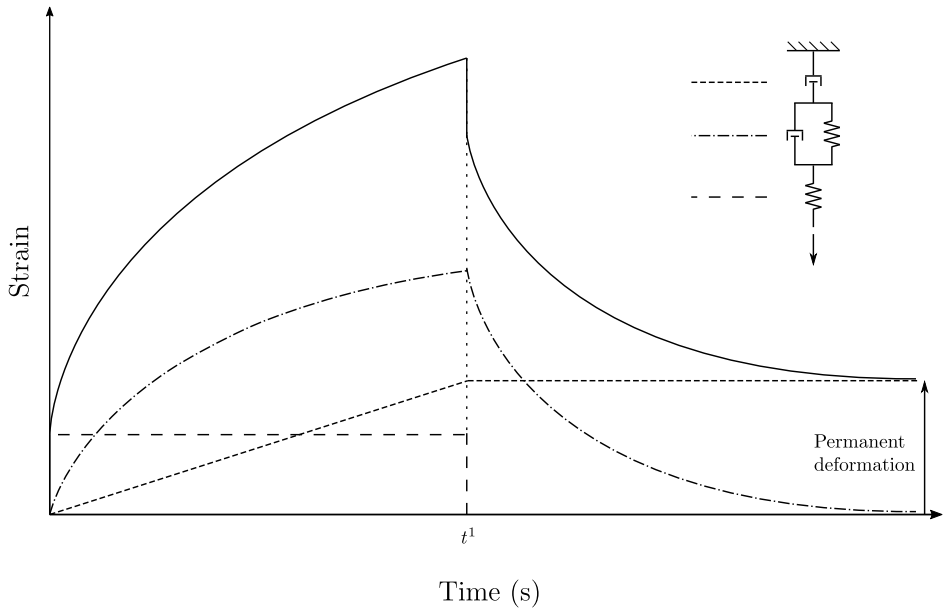

Figure 4-2: Deformation of the Burgers element, which is a linear version of the ice element used here, and its components when applying an instantaneous stress at $t = 0\,\mathrm{s}$ and instantaneous removal at $t = t^1$. The dashed lines show the strain curves for each part as indicated in the sketch at the upper right. The solid line indicates the strain of the entire element, at the point where the stress is applied.

creep or Glen's law, as described by Ponter et al. (1983), Weertman (1983) and Løset et al. (1998):

$$\dot{\varepsilon} \sim \sigma^3. \tag{4-1}$$

The remainder of the element is the crushing part, with spring K_2 and spring K_1 in parallel with dashpot C_1.

Spring K_2 accounts for local brittle fracture. When the indentation of the spring is equal to the maximum admissible value δ_{crit} (in meters),

$$x_{i,2} - x_{i,1} = \delta_{\mathrm{crit}}, \tag{4-2}$$

the element breaks and is removed from the interface. A new element is placed at a distance from the structure edge at time of fracture ($x_{\mathrm{s}}(t_{\mathrm{frac}})$), which is drawn from a uniform distribution U:

$$x_{i,1} = x_{i,2} = x_{i,3} = x_{\mathrm{s}}(t_{\mathrm{frac}}) - U\left(0, r_{\mathrm{max}}\right), \tag{4-3}$$

where r_{max} is the maximum offset of an element with respect to the structure (in meters).

The middle part, with the spring and dashpot in parallel, accounts for element deformation in the transitional regime of velocities. In rheology, this element is called the Kelvin-Voigt element and captures delayed elastic deformation (Sanderson, 1988).

Altogether, the element mimics the viscoelastic behavior of ice. In rheological theory, the linear version of this element, with linear creep and without failure, is referred to as the Burgers model. Its deformation after application of an instantaneous stress is sketched in Figure 4-2, including the behavior of each component separately.

By removing the ice elements from the model after breakage, it is assumed that ice is cleared from the interface and will not accumulate in front of the structure, omitting forces exerted by the ice rubble and assuming direct contact between ice and structure (Dempsey et al., 2001).

4-2 Equations of motion

As can be deduced from Equation 4-3, the element has no length as all nodes have the same initial location in non-contact. The equations of motion for the nodes are given by:

$$x_{i,1} = \begin{cases} x_{i,2}, & \text{if } x_{i,1} \quad < x_\mathrm{s} \quad \text{(no contact)} \\ x_\mathrm{s}, & \text{if } x_{i,1} \quad \geq x_\mathrm{s} \quad \text{(contact)} \end{cases}, \tag{4-4}$$

$$\dot{x}_{i,2} = \frac{K_2}{C_1}\left(x_{i,1} - x_{i,2}\right) + \frac{K_1}{C_1}\left(x_{i,3} - x_{i,2}\right) + v_\mathrm{ice} - \left(\frac{K_2}{C_2}\left(x_{i,2} - x_{i,1}\right)\right)^3, \tag{4-5}$$

$$\dot{x}_{i,3} = v_\mathrm{ice} - \left(\frac{K_2}{C_2}\left(x_{i,2} - x_{i,1}\right)\right)^3, \tag{4-6}$$

where $x_{i,1}$, $x_{i,2}$, $x_{i,3}$ are the displacements of the element nodes in meters, overdots indicate their velocities (in meters per second). x_s is the structural displacement (in meters) at the point of ice action and v_ice the velocity of ice (in $\mathrm{m\,s^{-1}}$). The latter is considered constant, as a large mass and inertia are assumed. Therefore, the loss of mass is negligible and driving forces are not taken into account (Hendrikse et al., 2018).

The total force exerted by the ice on the structure F_ice (global ice force in newton) is the sum of all N forces in springs K_2:

$$F_\mathrm{ice} = \sum_{i=1}^{N} K_2\left(x_{i,2} - x_{i,1}\right), \tag{4-7}$$

where it is assumed that the force of all ice elements act at one point of the structure. The implementation of failure of the element is explained in Section 5-5.

4-3 Ice parameters

The parameters of the elements (N, K_1, K_2, C_1, C_2, δ_crit and r_max) are derived from measurement data, as described by Hendrikse et al. (2018). Since uniformity of ice is assumed, these parameters are identical in each ice element.

The ice properties that are being varied in this research on ice-induced vibrations (IIV) are the ice velocity (v_ice) and ice thickness (h). As no wind turbine installations are planned for the Arctic region, the range for ice thickness and velocity are taken from measurements in the southern Baltic Sea in the Subarctic, where wind farms are already under construction and more being developed. Gravesen and Kärnä (2009) reported that the thickest ice floes measured in the Baltic area are 0.48 m thick. Leppäranta (1981) reported an ice thickness of 0.5 m in this area, so this value is taken as the maximum thickness in this research. Besides, in Lepparanta's research on the drift of sea ice, a velocity up to $0.4\,\mathrm{m\,s^{-1}}$ under the influence of currents and winds was found. A conservative maximum value of $0.5\,\mathrm{m\,s^{-1}}$ is used here. The input parameters for the ice model are summarized in Table 4-1.

Table 4-1: Ice parameters for ice acting on a jacket leg with diameter $d = 1.2\,\mathrm{m}$.

Parameter	**Value**	**Unit**
N	38	-
K_1	3.753	$\mathrm{MN\,m^{-1}}$
K_2	18.414	$\mathrm{MN\,m^{-1}}$
C_1	14.878	$\mathrm{MN\,s\,m^{-1}}$
C_2	0.368	$\mathrm{MN\,s\,m^{-1}}$
δ_{crit}	0.002	m
r_{max}	0.006	m
h_{ice}	$(0.1, 0.2, 0.3)$	m
v_{ice}	$(0.005, 0.01, \ldots, 0.5)$	$\mathrm{m\,s^{-1}}$

Chapter 5

Numerical implementation

In this section, the implementation of the previously explained models for ice and structure is discussed. Instead of solving the system of equations 3-1 of the structure in the time domain (or nodal/spatial domain), it is desired to solve it in the modal domain, because of three advantages. First, the structural equations of motion will decouple, resulting in a set of differential equations that can be solved separately. Second, modal damping can be implemented; the damping of the system can be set per mode separately. Third, the solution space can be truncated, yielding a smaller set of equations that need to be solved, which results in a reduction of simulation time.

These advantageous properties of the modal domain are further elaborated in Sections 5-1, 5-2 and 5-3. For a more comprehensive explanation of computation in the modal domain, the reader is referred to the literature, for example Géradin and Rixen (2015) and Chopra (2015), on which this chapter is based. As the equations of motion of the ice elements are still modeled in the spatial domain, a coupling between the two domains is made. The implementation of this coupling is explained in Sections 5-4 and 5-5. After that, a flowchart illustrating the structure of the code is given in Section 5-6. The chapter finishes with an error estimation of the truncated structural model in Section 5-7.

5-1 Mode superposition

Assuming a harmonic free vibration motion with frequency ω, the eigenvalue problem of dynamic system 3-1 without damping reads:

$$\mathbf{K}\boldsymbol{\phi}_i = \omega_i^2 \mathbf{M}\boldsymbol{\phi}_i, \tag{5-1}$$

the solution of which yields the N_s eigenfrequencies ω_i and the corresponding eigenvectors $\boldsymbol{\phi}_i$.

These N_s eigenmodes form a complete basis to express the structural dynamic behavior, meaning that any vector in the solution space can be represented as a linear combination of

the eigenmodes. Therefore, the solution to the equations of motion of the structure (Equation 3-1) can be written as

$$\mathbf{x}(t) = \sum_{i=1}^{N_\mathrm{s}} \boldsymbol{\phi}_i \eta_i(t) = \boldsymbol{\Phi}\boldsymbol{\eta}(t) = \begin{bmatrix} | & | & & | \\ \boldsymbol{\phi}_1 & \boldsymbol{\phi}_2 & \dots & \boldsymbol{\phi}_{N_\mathrm{s}} \\ | & | & & | \end{bmatrix} \begin{bmatrix} \eta_1 \\ \eta_2 \\ \vdots \\ \eta_{N_\mathrm{s}} \end{bmatrix}, \tag{5-2}$$

in which η_i and $\boldsymbol{\eta}$ are the modal displacement of mode i and the modal displacement vector, respectively. Matrix $\boldsymbol{\Phi}$ is the eigenmatrix, containing the eigenmodes in its columns. From now on, the time dependence is omitted in the descriptions for convenience.

5-2 Modal decoupling

Substituting Equation 5-2 into 3-1, pre-multiplying with the transpose of the eigenmatrix yields

$$\underbrace{\boldsymbol{\Phi}^\mathsf{T}\mathbf{M}\boldsymbol{\Phi}}_{\mathbf{M}^*}\ddot{\boldsymbol{\eta}} + \underbrace{\boldsymbol{\Phi}^\mathsf{T}\mathbf{C}\boldsymbol{\Phi}}_{\mathbf{C}^*}\dot{\boldsymbol{\eta}} + \underbrace{\boldsymbol{\Phi}^\mathsf{T}\mathbf{K}\boldsymbol{\Phi}}_{\mathbf{K}^*}\boldsymbol{\eta} = \underbrace{\boldsymbol{\Phi}^\mathsf{T}\mathbf{f}}_{\mathbf{f}^*}. \tag{5-3}$$

From Equation 5-1 it follows that the eigenmodes are orthogonal with respect to the mass and stiffness matrices (see derivation in Appendix A), resulting in diagonality of modal matrices $\mathbf{M}^*$ and $\mathbf{K}^*$. Since the damping in the structure is defined either as damping per mode or as a linear combination of the mass and stiffness matrices, the modal damping matrix $\mathbf{C}^*$ is diagonal as well. Mass-normalization of the eigenmodes results in the decoupled normal equations that need to be solved for the modal amplitudes η:

$$\mathbf{M}^*\ddot{\boldsymbol{\eta}} + \mathbf{C}^*\dot{\boldsymbol{\eta}} + \mathbf{K}^*\boldsymbol{\eta} = \mathbf{f}^*, \tag{5-4}$$

$$\mathbf{M}^* = \begin{bmatrix} 1 & & & \\ & 1 & & \\ & & \ddots & \\ & & & 1 \end{bmatrix}, \tag{5-5}$$

$$\mathbf{C}^* = \begin{bmatrix} 2\zeta_1\omega_1 & & & \\ & 2\zeta_2\omega_2 & & \\ & & \ddots & \\ & & & 2\zeta_n\omega_{N_\mathrm{s}} \end{bmatrix}, \tag{5-6}$$

$$\mathbf{K}^* = \begin{bmatrix} \omega_1^2 & & & \\ & \omega_2^2 & & \\ & & \ddots & \\ & & & \omega_{N_\mathrm{s}}^2 \end{bmatrix}. \tag{5-7}$$

where ζ_i represents the modal damping ratio. Depending on the damping model, the values of ζ_i follow the graph in Figure 3-4; they are all equal to 0.01 in the modal damping case, and growing after the second distinct eigenfrequency for the Rayleigh damping model.

5-3 Modal truncation

Since frequency lock-in is reported to occur up to 10 Hz, calculating the response of all $N_\mathrm{s} = 414$ vibration modes, which range up to 5300 Hz, is overabundant. Therefore, the model can be reduced by considering only the first $k < N_\mathrm{s}$ modes, using the so-called *Modal Displacement Method*, resulting in a considerably shorter simulation time. The summation of modes (Equation 5-2) is truncated and the solution for the displacement is approximated:

$$\mathbf{x} \approx \sum_{i=1}^{k} \boldsymbol{\phi}_i \eta_i = \boldsymbol{\Phi}_\mathrm{t} \boldsymbol{\eta}_\mathrm{t} = \mathbf{x}_\mathrm{t}, \tag{5-8}$$

where $\mathbf{x}_\mathrm{t}$ is the solution using the truncated model. $\boldsymbol{\Phi}_\mathrm{t}$ and $\boldsymbol{\eta}_\mathrm{t}$ are the truncated eigenmatrix and modal displacement vector. Substituting this equation into Equation 3-1 again gives:

$$\mathbf{M}\boldsymbol{\Phi}_\mathrm{t}\ddot{\boldsymbol{\eta}}_\mathrm{t} + \mathbf{C}\boldsymbol{\Phi}_\mathrm{t}\dot{\boldsymbol{\eta}}_\mathrm{t} + \mathbf{K}\boldsymbol{\Phi}_\mathrm{t}\boldsymbol{\eta}_\mathrm{t} = \mathbf{f} + \mathbf{r}. \tag{5-9}$$

Since the model does not contain the higher frequency modes, the inertia forces, damping forces and internal stresses of the structure are not fully in equilibrium with the external forces $\mathbf{f}$, and a residual force $\mathbf{r}$ remains. As the eigenvectors in $\boldsymbol{\Phi}_\mathrm{t}$ are orthogonal to the omitted eigenvectors, $\boldsymbol{\Phi}_\mathrm{t}^\mathsf{T}\mathbf{r} = \mathbf{0}$, pre-multiplication of Equation 5-9 by $\boldsymbol{\Phi}_\mathrm{t}^\mathsf{T}$ yields the reduced set of equations of motion (Cook et al., 2012; Van der Seijs, 2016):

$$\underbrace{\boldsymbol{\Phi}_\mathrm{t}^\mathsf{T}\mathbf{M}\boldsymbol{\Phi}_\mathrm{t}}_{\mathbf{M}_\mathrm{t}^*}\ddot{\boldsymbol{\eta}}_\mathrm{t} + \underbrace{\boldsymbol{\Phi}_\mathrm{t}^\mathsf{T}\mathbf{C}\boldsymbol{\Phi}_\mathrm{t}}_{\mathbf{C}_\mathrm{t}^*}\dot{\boldsymbol{\eta}}_\mathrm{t} + \underbrace{\boldsymbol{\Phi}_\mathrm{t}^\mathsf{T}\mathbf{K}\boldsymbol{\Phi}_\mathrm{t}}_{\mathbf{K}_\mathrm{t}^*}\boldsymbol{\eta}_\mathrm{t} = \underbrace{\boldsymbol{\Phi}_\mathrm{t}^\mathsf{T}\mathbf{f}}_{\mathbf{f}_\mathrm{t}^*}. \tag{5-10}$$

5-4 State space representation

To be able to combine the truncated structural model with the ice model and use a single solver in MATLAB for all differential equations, the k second order equations of the structure are rewritten to $2k$ first order equations. This is done using the state space representation for the modal displacements η_t, by substituting the state vector

$$\mathbf{z} = \begin{bmatrix} \boldsymbol{\eta}_\mathrm{t} \\ \dot{\boldsymbol{\eta}}_\mathrm{t} \end{bmatrix}_{2k\times 1} \tag{5-11}$$

into the system of equations 5-10 (Genta, 2012). Rewriting yields the following set of first order differential equations:

$$\dot{\mathbf{z}} = \begin{bmatrix} \dot{\boldsymbol{\eta}}_\mathrm{t} \\ \ddot{\boldsymbol{\eta}}_\mathrm{t} \end{bmatrix} = \underbrace{\begin{bmatrix} \mathbf{0} & \mathbf{I} \\ -\mathbf{K}_\mathrm{t}^* & -\mathbf{C}_\mathrm{t}^* \end{bmatrix}}_{\mathbf{A}} \begin{bmatrix} \boldsymbol{\eta}_\mathrm{t} \\ \dot{\boldsymbol{\eta}}_\mathrm{t} \end{bmatrix} + \underbrace{\begin{bmatrix} \mathbf{0} \\ \boldsymbol{\Phi}_\mathrm{t}^\mathsf{T} \end{bmatrix}}_{\mathbf{B}} \mathbf{f}, \tag{5-12}$$

where each block of matrix $\mathbf{A}$ is either zero or diagonal. The ice force $\mathbf{f}$ is a function of the relative motion between the structure and ice (see Equation 4-7). Here, the coupling between the two models comes into play, which will be discussed in the next section.

5-5 Coupling of ice and structure

Now that the number of structural equations is reduced and the equations are rewritten to fist order, the coupling with the ice model can be made. The force acting on the structure is a function of the indentation of the ice elements, which in its turn is a function of the structural displacement at sea level, as described by x_s in Equations 4-4 to 4-6. Since the structural displacement is computed in the modal domain, the modal displacements η_i need to be transfered to the spatial domain to allow them to be inserted into the ice equations of motion. This transformation is performed using Equation 5-8. When the ice force is acting on degree of freedom x_p, the structural displacement at this point is found by the multiplication of row p of eigenmatrix $\mathbf{\Phi}_\mathrm{t}$ by the vector of modal displacements $\boldsymbol{\eta}_\mathrm{t}$, as outlined in the following equation:

$$x_\mathrm{s} = \begin{bmatrix} | \\ \boldsymbol{x} \\ | \\ \boxed{x_p} \\ | \end{bmatrix} = \begin{bmatrix} | & | & & | \\ \boldsymbol{\phi}_1 & \boldsymbol{\phi}_2 & \cdots & \boldsymbol{\phi}_k \\ | & | & & | \\ \boxed{\phi_{p,1} \;\; \phi_{p,2} \;\; \cdots \;\; \phi_{p,k}} \\ | & | & & | \end{bmatrix} \begin{bmatrix} \eta_1 \\ \eta_2 \\ \vdots \\ \eta_k \end{bmatrix} = \mathbf{\Phi}_{\mathrm{t},p} \boldsymbol{\eta}_\mathrm{t}, \tag{5-13}$$

which yields the value of x_s that needs to be substituted in the equations for the ice elements (Equations 4-4 to 4-6) and the equation for the ice force (Equation 4-7). The latter yields the entry of the force vector $\mathbf{f}$ in Equation 5-12 at degree of freedom p:

$$f_p = F_\mathrm{ice}\left(x_p\right) = \sum_{i=1}^{N} K_2 \left(x_{i,2} - \mathbf{\Phi}_{\mathrm{t},p} \boldsymbol{\eta}_\mathrm{t}\right) H \left(x_{i,2} - \mathbf{\Phi}_{\mathrm{t},p} \boldsymbol{\eta}_\mathrm{t}\right), \tag{5-14}$$

where the conditional statement for contact is replaced by the Heaviside step function.

5-6 Flowchart of code

The code solving the coupled model is implemented in MATLAB. Its structure is illustrated in Figure 5-1. After initializing the ice and structure, the model is solved using the `ode45` solver with event location to handle failure events. The equations of motions are solved until one of the ice elements breaks, which is then set back to a new position from the structure at time of fracture. This time of fracture is the starting point for the next iteration. This process repeats until the time of fracture exceeds the total simulation time $t_{\max}$. Then, the simulation is stopped and the displacements, velocities and forces are outputted.

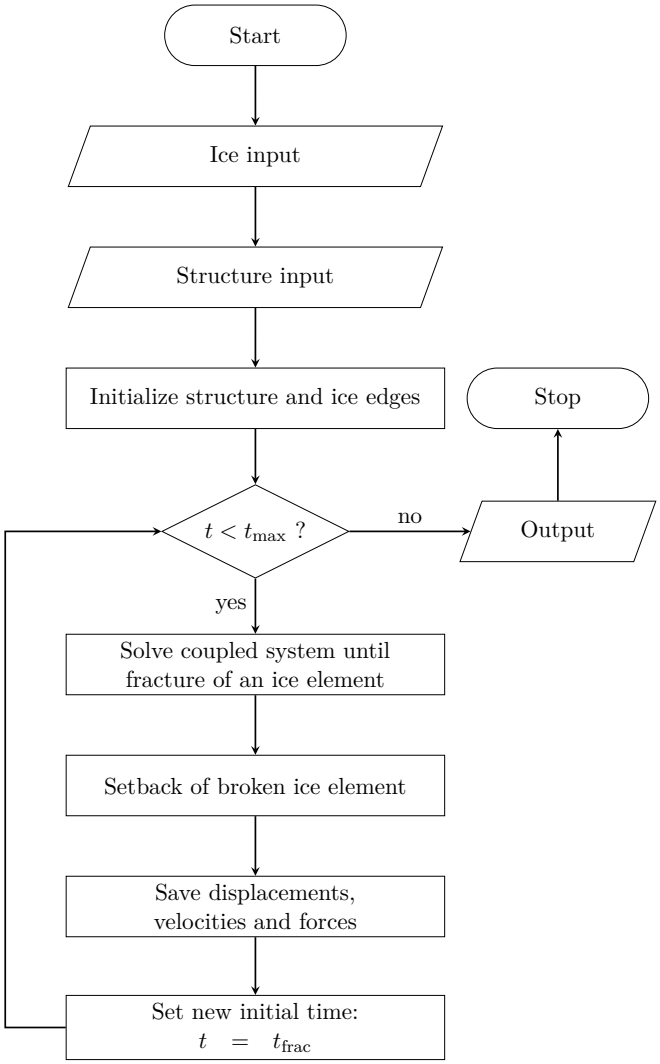

Figure 5-1: Flowchart of the code that solves the coupled system of equations.

5-7 Error estimation

To judge how many modes or which frequencies need to be incorporated in the model, the quality of the structural modal truncation is measured using a global relative error (GRE) defined as (Farhat et al., 2014):

$$\frac{\sqrt{\sum_{t\in P}\left(x(t)-x_{\mathrm{t}}(t)\right)^{\mathsf{T}}\left(x(t)-x_{\mathrm{t}}(t)\right)}}{\sqrt{\sum_{t\in P}x(t)^{\mathsf{T}}x(t)}}\cdot 100\,\%, \tag{5-15}$$

where P is the set of time instances for which the relative error is evaluated. The GRE is computed for the x- and y-displacements at the nodes at sea level, for 2000 time instances and two load cases: one where one leg of the structure is loaded, and one where the two front legs experience an ice force, both in x-direction. When including modes up to 50 Hz, far above the expected range for frequency lock-in (FLI), the error in the direction of ice movement is less than 1.5 % for all time instances. The error perpendicular to ice movement (y-displacements) has a maximum of 10 %. However, this perpendicular displacement does not interact with the ice and is more than 10 times smaller than the displacement in ice direction, so it is considered sufficiently accurate. From now on, the reduced order model containing eigenmodes up to 50 Hz is used.

Chapter 6

Load cases

In this chapter, the four studied load cases of ice acting on the wind turbine on a jacket foundation are explained. In the first load case, the effect of ice on the occurrence of ice-induced vibrations (IIV) is studied as a function of ice thickness and ice velocity. The second load case tests the effect of the used damping model, using the two damping models described in Sections 3-3 and 5-2. Thirdly, the angle of approach (or angle of incidence) of ice is varied. In this load case, the excitation of the first rotational mode is tested as well by applying a load to only one leg. In all previous load cases, the effect of ice is studied solely. In the fourth case, an aerodynamic force is applied to the rotor and nacelle assembly (RNA) to assess whether the aerodynamic effects during operation are beneficial to IIV or not, considering the worst case scenario from the previous mentioned load cases.

The implementation of angle of approach and aerodynamic forces is described in more detail in the next sections.

6-1 Angle of approach

Due to symmetry of the structural model, the range of unique load cases reduces to one-eighth of the total range of 360°. The angles of approach are given between 0° to 45°, as sketched in Figure 6-1a.

For certain angles of approaching ice, the rear legs of the structure are not or less loaded by the ice due to shielding by the front ones. For example, for ice approaching perpendicular to one of the faces of the structure, at 0° (see Figure 6-1a), the two rear legs are not loaded at all. In the range of 15.3° to 34.2°, no legs are shielded and the ice acts on all four legs. For an angle of 45°, one leg is shielded. Throughout this research, the effect of ice on the braces of the jacket is not considered. The results are given in Section 8-3.

To check if the rotational mode of the structure can be excited (Figure 3-5c), the ice model is applied to only one leg, at 45°, as sketched in Figure 6-1b. The results are presented in Section 8-4.

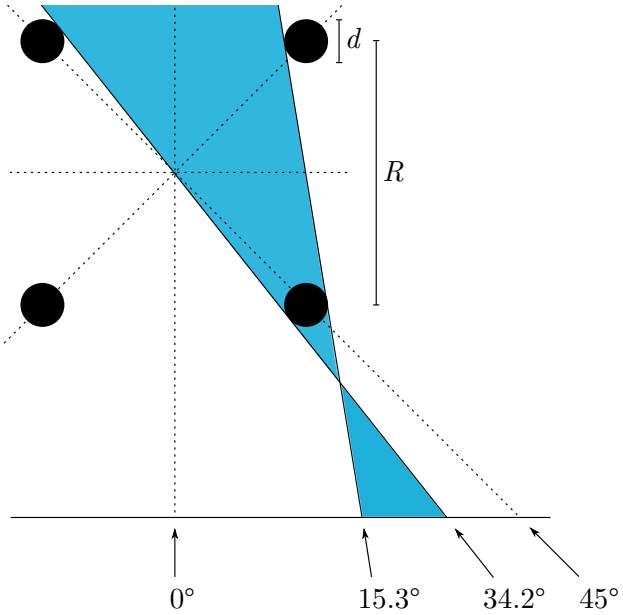

(a) Schematic drawing of shielding and symmetry of the structure. The blue area indicates the range of angles of the ice for which all four legs of the jacket are loaded, between 15.3° and 34.2°, calculated using the diameter of the legs ($d = 1.2\,\text{m}$) and the distance between them ($R = 9.06\,\text{m}$).

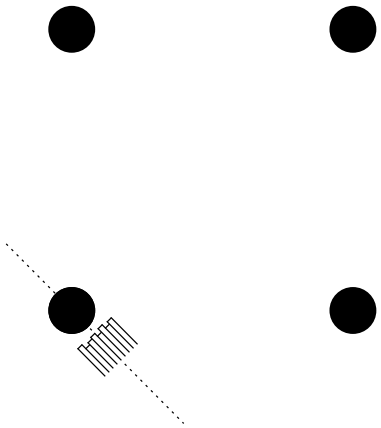

(b) Illustration of the load case with which the excitation of the rotational mode is tested: one loaded leg under an angle of 45°.

Figure 6-1: Schematic drawing of the load cases for different angles of approaching ice, using the cross section of the jacket structure at water level. The black circles represent the legs of the structure. Due to the symmetry in the system (indicated by the dashed lines), only a range of angles of 45° needs to be taken into account in the load cases to cover all possible configurations.

6-2 Aerodynamic loading

While the wind turbine is operating, aerodynamic forces act on the structure. The one that might influence the ice-induced vibrations is the thrust force, which acts on the structure at the RNA, in the direction perpendicular to the rotor plane. In this load case, a simplified thrust force is applied to the top of the structure to test the effect of wind loading on ice-induced vibrations. The thrust force time series are taken from simulations of a representative wind farm.

Thrust time series for two wind speeds are generated. The first one is the cut-in wind speed of $3\,\mathrm{m\,s^{-1}}$; the lowest speed at which the wind turbine generates electrical power. The second one is at $12\,\mathrm{m\,s^{-1}}$, which is at rated wind speed, the speed at which the power production is at its maximum. When the wind speed exceeds the rated wind velocity, the turbine pitches its blades to keep the rotational speed constant.

As the full thrust time series is confidential, the normalized versions for the two wind speeds are depicted in Figure 6-2. The force time series are applied in the direction of the ice force, since this is the direction in which it can affect the ice-induced vibrations most.

Simulations are performed both with and without aerodynamic damping. It is implemented in a simplified manner; constant damping values are taken from the previously mentioned wind farm simulations and added to the existing damping values. This is done for the first three structural bending modes. The values could not be reported here, as they are confidential. The results are given in Section 8-6.

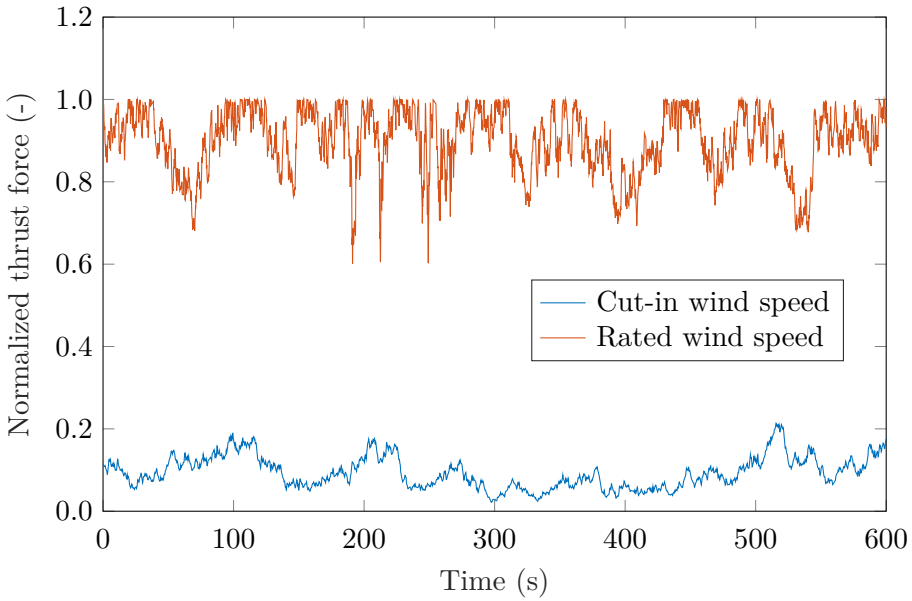

Figure 6-2: Normalized thrust force time series for cut-in wind speed ($3\,\mathrm{m\,s^{-1}}$) and rated wind speed ($12\,\mathrm{m\,s^{-1}}$).

Chapter 7

Post-processing: identification of ice-induced vibration regimes

In all ice models discussed in Section 2-3-2, a single degree-of-freedom oscillator is used to represent the structural motion. Therefore, the structure moves in one mode only and the intermittent crushing (IC) and frequency lock-in (FLI) regimes are relatively easy to distinguish, as in Figure 2-4. In this study, however, a multi-modal jacket structure is used and the difference between the two vibration regimes is not so distinct. The goal is to find the two transition velocities; from intermittent crushing to frequency lock-in and from frequency lock-in to continuous brittle crushing, as illustrated in Figure 2-3. In the single-degree-of freedom model, a graph of maximum velocity of the structure as a function of ice velocity was used to determine the FLI regime. However, it can not be used in a multi-modal model, since the velocity at sea level is determined by many modes. Here, two characteristics of the regimes are defined from observations, which are used to analyze and categorize the ice-structure interaction: the maximum displacement and the fundamental frequency. They are discussed in Sections 7-1 and 7-2, respectively. The automated identification of the crushing regimes is shortly discussed in Section 7-3.

7-1 Maximum displacement

The first and most explicit distinction between IC, FLI and continuous brittle crushing (CBR) is the displacement at sea level, as explained in Section 2-2. At low ice velocities, the force builds up and the maximum displacements are large. Then, at a certain higher ice velocity, the FLI regime can start, where the maximum displacements are small at first, but grow with increasing ice velocities. The CBR regime starts at the second transition velocity. The forces acting on the structure are small compared to the other two regimes, and as the force is not locked in with one of the modes, a small structural displacement at sea level tells the CBR regime apart from the other two. In Figures 7-1, 7-2 and 7-3, typical simulated displacements for the IC, FLI and CBR regimes are depicted.

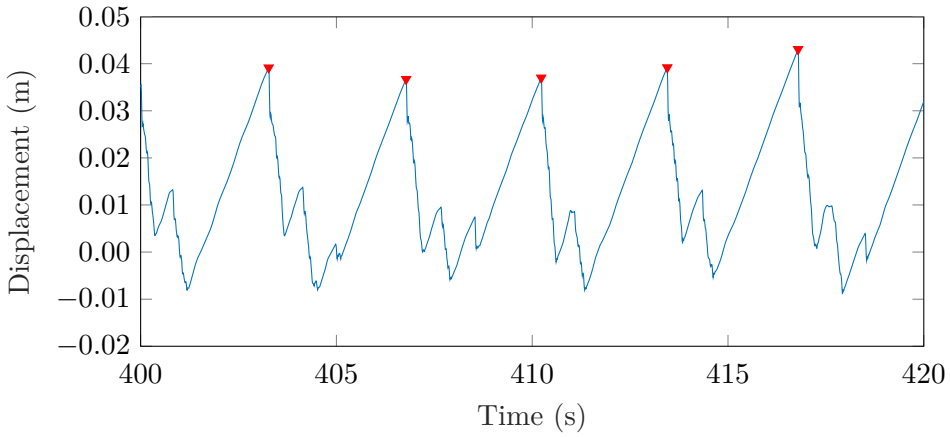

Figure 7-1: Time series of the displacement in ice direction of node 44, due to approaching ice of 0.5 m thick, under an angle of 5° and with a velocity of 0.025 m s^{-1}, which is in the IC regime.

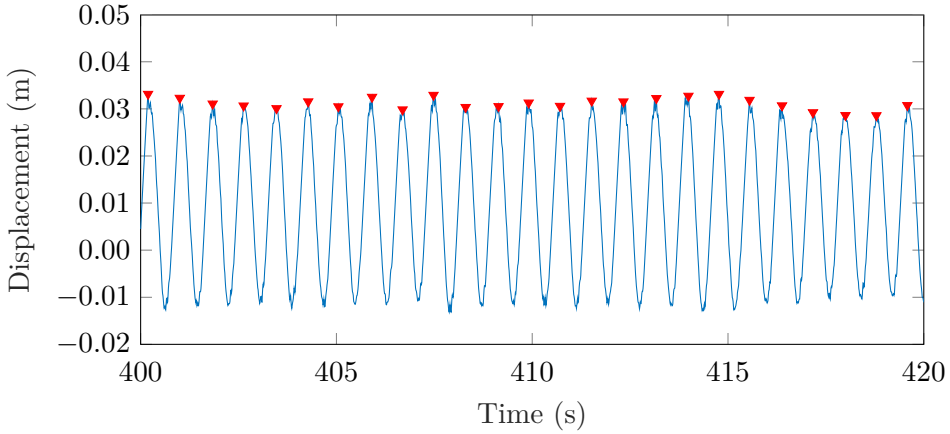

Figure 7-2: Time series of the displacement in ice direction of node 44, due to approaching ice of 0.5 m thick, under an angle of 5° and with a velocity of 0.160 m s^{-1}, which is in the FLI regime.

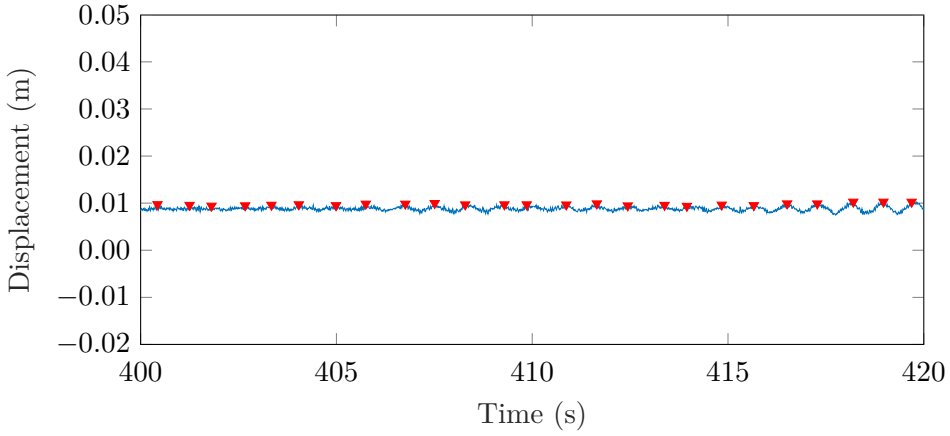

Figure 7-3: Time series of the displacement in ice direction of node 44, due to approaching ice of 0.5 m thick, under an angle of 5° and with a velocity of 0.300 m s^{-1}, which is in the CBR regime.

To give the maximum displacement a quantitative measure, the `findpeaks` tool in MATLAB is used. Simulations of 600 seconds are performed, however, only data from 300 to 600 seconds is considered in order to reduce the transient effect of the initial conditions. The identified peaks, which are indicated by red markers in Figures 7-1, 7-2 and 7-3, are averaged and the values are plotted for each ice velocity. This results in Figure 7-4, where the average maximum displacements are plotted versus the ice velocity for a specific case. The two transitions between crushing regimes are observed.

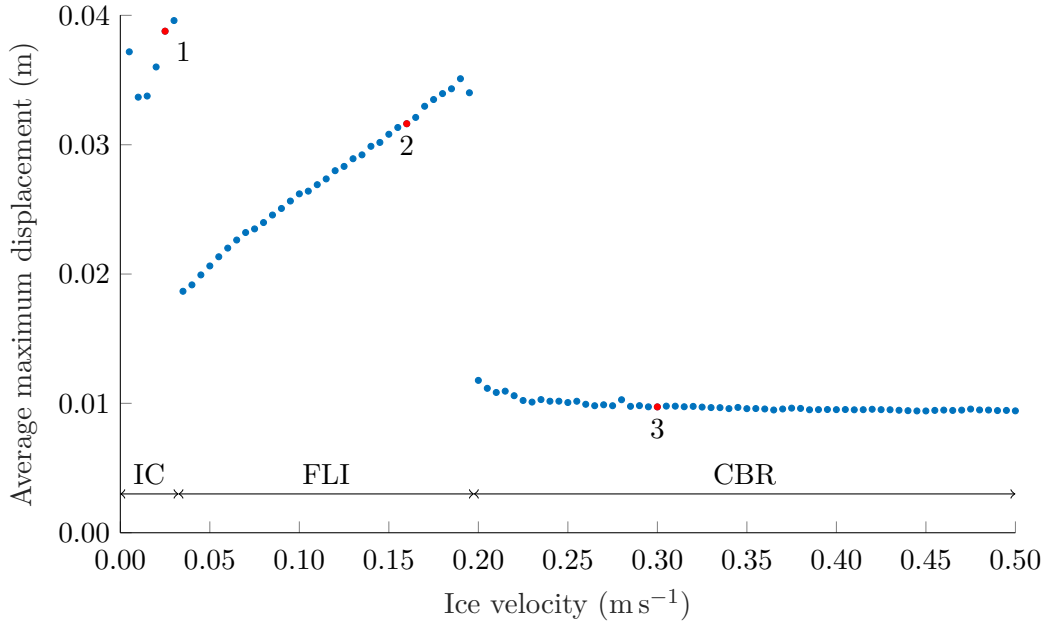

Figure 7-4: Graph of the average maximum structural displacement of node 44 versus ice velocity. The load case is: ice of 0.5 m thick, approaching under and angle of 5°, causing a force on the two front legs. The three crushing regimes can be distinguished. Point 1 is in the intermittent crushing regime, point 2 in the frequency lock-in regime and point 3 in the continuous brittle crushing regime. Parts of the time series are plotted in Figures 7-1, 7-2 and 7-3, respectively.

As shown in the graph, the average maximum displacements are high in the intermittent crushing regime. Then, the maximum displacement drops, between $v_{\text{ice}} = 0.03\,\text{m}\,\text{s}^{-1}$ and $0.035\,\text{m}\,\text{s}^{-1}$ in this case, where after the FLI regime starts. The maximum displacements grow more or less linearly within this regime, until the transition to CBR, where the maximum displacement drops again between $v_{\text{ice}} = 0.19\,\text{m}\,\text{s}^{-1}$ and $0.20\,\text{m}\,\text{s}^{-1}$. The ice no longer locks in with the movement of the structure.

7-2 Fundamental frequency

Another way to distinguish the intermittent crushing regime from the frequency lock-in regime is by means of autocorrelation. The displacement signal is correlated with a shifted version of itself, resulting in a signal of correlation value as a function of time delay. Using this graph, the frequency of repeating patterns is found, called the fundamental frequency. This fundamental frequency is plotted for each ice velocity in Figure 7-5.

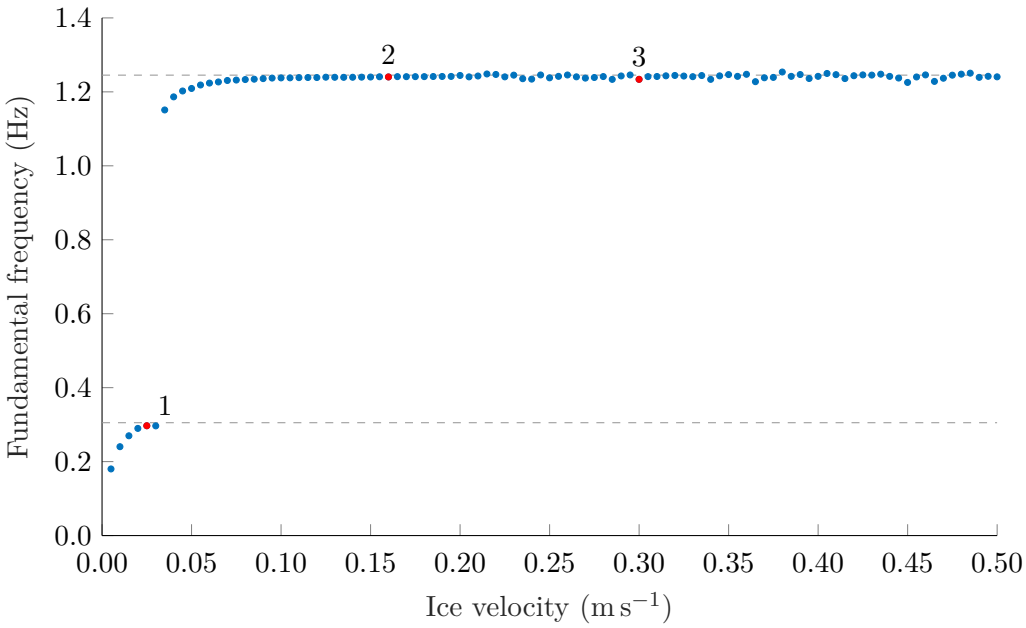

Figure 7-5: Graph of the fundamental frequency (of the displacement of node 44) versus ice velocity for the load case: ice of 0.5 m thick, approaching under and angle of 5°, causing a force on the two front legs. The dotted gray lines indicate the first and second natural frequencies of the structure.

Using the fundamental frequency, only two regimes can be identified. For low ice velocities, in the intermittent crushing regime, the fundamental frequency is low, below the first eigenfrequency of the structure. The fundamental frequency increases suddenly at the same transition velocity as before, between $0.030\,\mathrm{m\,s^{-1}}$ and $0.035\,\mathrm{m\,s^{-1}}$, and approaches the second eigenfrequency. Here, the ice force is locked in with the second normal mode of the structure. The transition to continuous brittle crushing can not be identified from this graph; the fundamental frequency stays close to the second natural frequency of the structure.

7-3 Automated identification of crushing regimes

Using the two previously explained properties, the crushing regimes can be identified. First, the start of the frequency lock-in regime is sought using the graph of the fundamental frequency. The fundamental frequency suddenly increases between intermittent crushing and frequency lock-in; the start of the frequency lock-in regime is found using this property. Then, the length of the frequency-lock in regime is extracted from the graph of average maximum displacements. Starting from the beginning of the frequency-lock in regime, the FLI regime can be identified using the fact that the maximum displacement is growing for higher ice velocities. Thereafter, the CBR regime starts.

Chapter 8

Results and discussion

This chapter explains the results of the simulations. The occurrence of ice-induced vibrations is studied as a function of ice thickness, applied damping model and angle of approaching ice. The vibrations are identified using the average maximum displacement and the fundamental frequency. A worst case scenario is found from the applied load cases, for both the displacements at water level and the displacements in the rotor and nacelle assembly (RNA) at the tower top. Finally, the effect of wind loading on the structure is studied. Throughout this chapter, simulations of different load cases are used to illustrate the phenomena. Various nodes at sea level are loaded by the ice, their numbers are indicated in Figure 3-6a.

8-1 Effect of ice thickness

First, the effect of ice thickness on the vibrations of the structure is examined. The average maximum displacement is plotted against ice velocity in Figure 8-1 for three ice thicknesses. For the whole range of ice velocities, the maximum displacements are larger for larger ice thicknesses. This is due to the fact that the ice is stronger; the stiffness and damping values in the ice elements are larger and the ice can therefore apply higher forces on the structure.

The second observation is that the frequency lock-in regime extends to larger ice velocities for thicker ice. This is due to the higher forces as discussed above. As the structure displaces further from its equilibrium, but with the same frequency, its velocity is larger. Therefore, the ice velocity at which the relative velocity between the structure and the ice is small is higher, extending the frequency lock-in (FLI) regime to higher velocities.

The source of the extension of the intermittent crushing (IC) regime for thicker ice, as can be seen in the figures, is harder to indicate. The derivation of the K_1 and C_1 values in the Kelvin-Voigt part of the ice element (see Figure 4-1b) leads to fluctuations of these values as a function of ice thickness. This influences the distribution of the internal displacements and therefore affects the moment of breakage of the ice element. Therefore, it is hard to define a trend and point out the effect of ice thickness on the extension of the IC regime. However, the point of onset of FLI does not change significantly as a function of ice thickness.

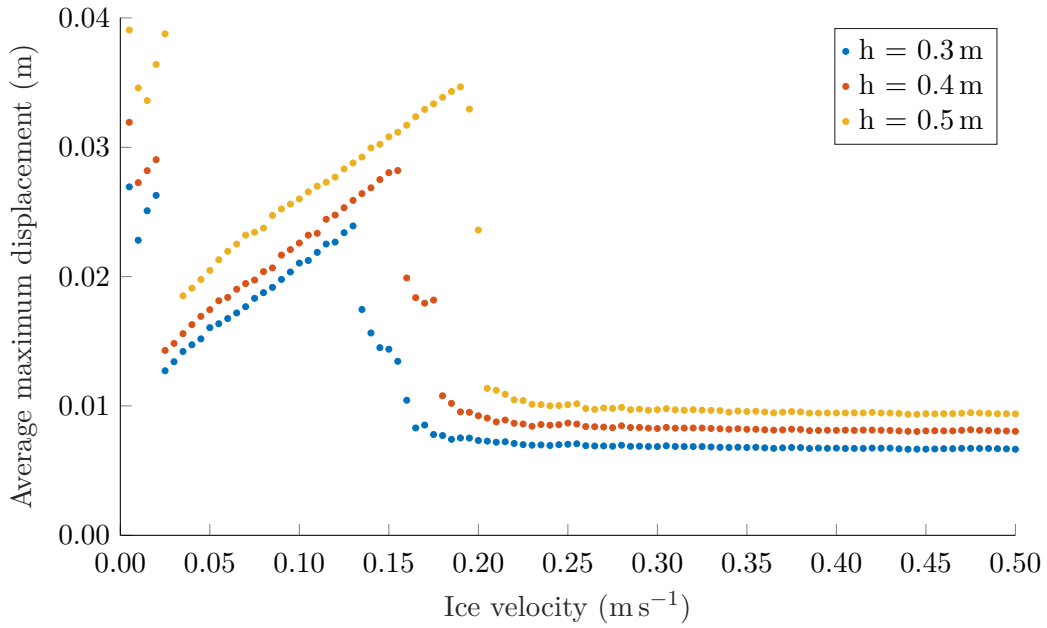

Figure 8-1: Graph of average maximum displacement versus ice velocity for the case where the two front legs are loaded, at 0°, for three different ice thicknesses h. The frequency lock-in regime extends to higher ice velocities for thicker ice.

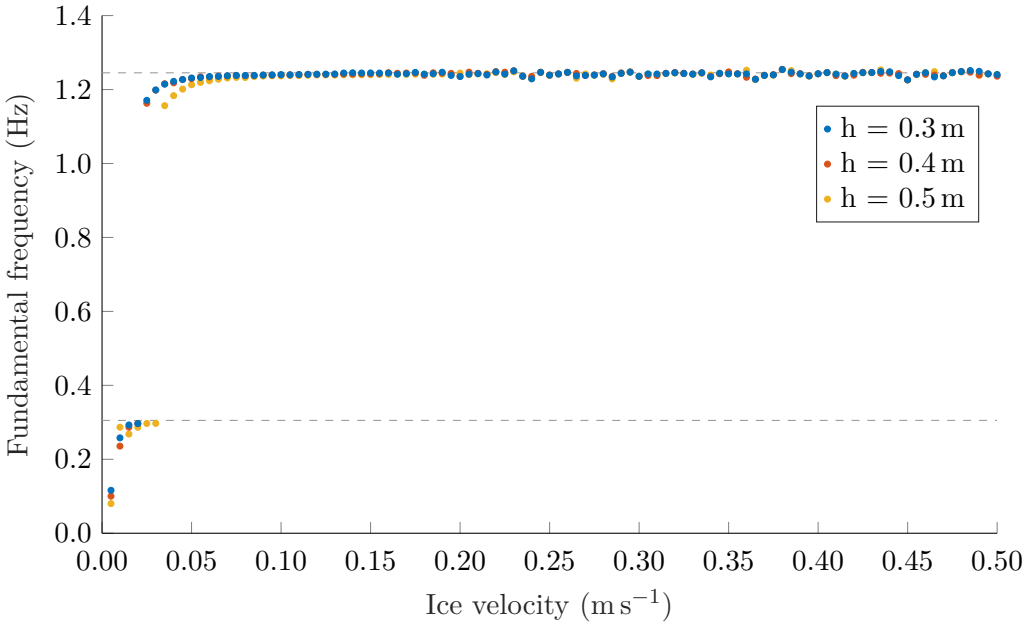

Figure 8-2: Graph of fundamental frequency versus ice velocity for the case where the two front legs are loaded, at 0°, for three different ice thicknesses.

8-2 Effect of damping

Next, the effect of damping is studied. Simulations are performed with Rayleigh and modal damping, as explained before. The maximum displacements are plotted in Figure 8-3, for a load case where all four legs are loaded. As shown in the figure, the frequency lock-in regime is shorter when using modal damping; the transition to continuous brittle crushing takes place at a lower ice velocity and the maximum displacements are lower.

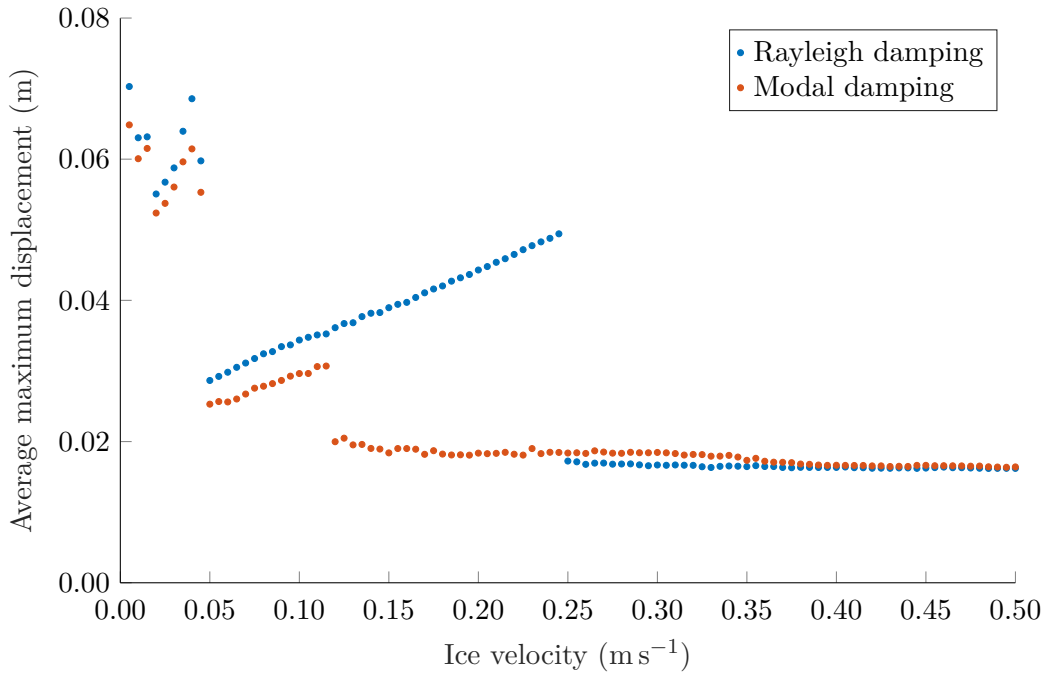

Figure 8-3: Plot of maximum displacement versus ice velocity for two types of damping: Rayleigh damping and modal damping. The Rayleigh damping is scaled for the first and second distinct eigenfrequency to 1 %. For modal damping, the damping of all modes is set to 1 %. Here, four legs were loaded under an angle of 15.3°.

This effect can be attributed to the fact that higher structural modes are less damped when using modal damping compared to Rayleigh damping. This hypothesis is supported by Figure 8-4, where the frequency response function (FRF) of the structure is plotted for modal damping and Rayleigh damping. The input and output are both taken at sea level. As can be seen, the structural displacement as a result of sinusoidal loading with frequencies between 17 and 21 Hz is significant when using modal damping, in contrast to the Rayleigh damping case. The eigenmodes in this range are triggered when the structure is excited at sea level. They have a relatively high modal displacement at sea level, as can be shown in Appendix B, where the modes are plotted.

These higher modes also appear in the autocorrelation function. An example is shown in Figure 8-5, where part of the autocorrelation is plotted for $v_{\text{ice}} = 0.385\,\text{m}\,\text{s}^{-1}$, in the continuous brittle crushing regime. Next to the fundamental frequency of 1.245 Hz (indicated by red dots), a 'superimposed' frequency is present in the signal (indicated by blue circles), of approximately 19 Hz in this case. Calculating the superimposed frequency for all ice veloc-

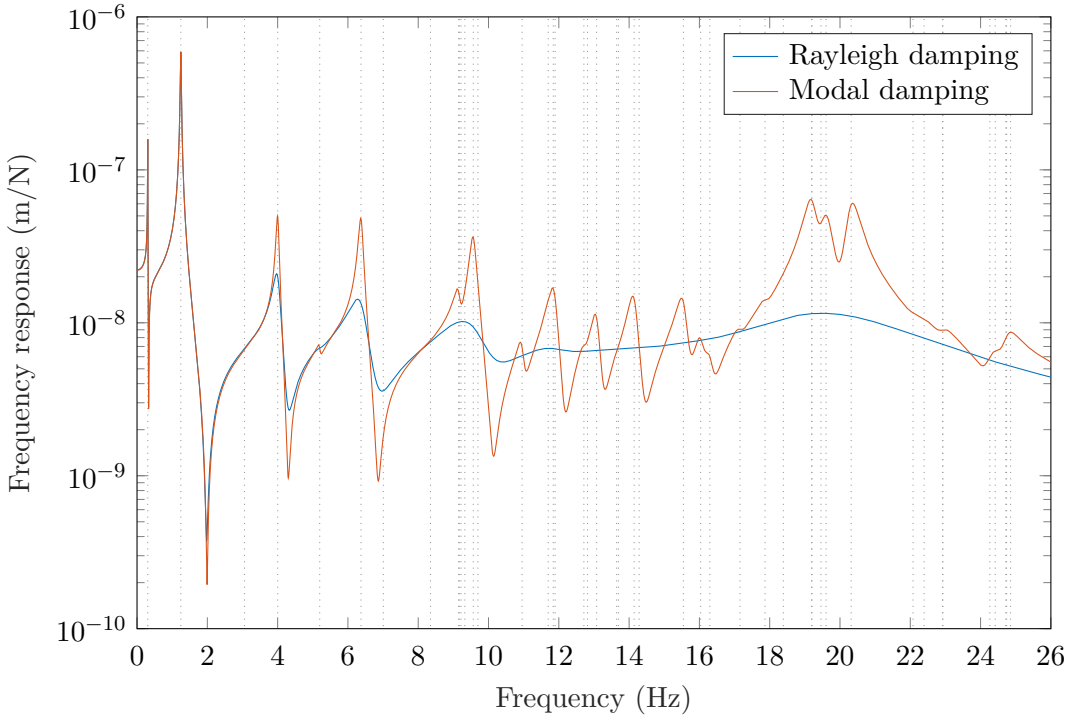

Figure 8-4: Graph of the frequency response function using two different damping models. Nodes 44 and 47 are loaded sinusoidally in-phase and the output at node 44 is plotted (at sea level). As can be seen, the damping in the modal damping model is lower and the modes around 20 Hz are contributing significantly to the response, in contrast to the Rayleigh damping case.

ities results in Figure 8-6. In this figure, it can be seen that these frequencies lie between approximately 17 and 21 Hz.

Lastly, simulations are carried out using eigenmodes of the structure up to 15, 17 and 18 Hz to check whether the eigenmodes in this range indeed affect the extension of the FLI regime. The plots for maximum displacement are depicted in Figure 8-7. As shown, when eigenmodes up to 17 Hz are incorporated in the structural model, frequency lock-in takes place for both damping models. However, the occurrence of FLI is distorted when the modes between 17 and 18 Hz are taken into account as well. It is concluded that the modes from 17 Hz can indeed distort the occurrence of FLI for higher ice velocities when the modal damping model is used.

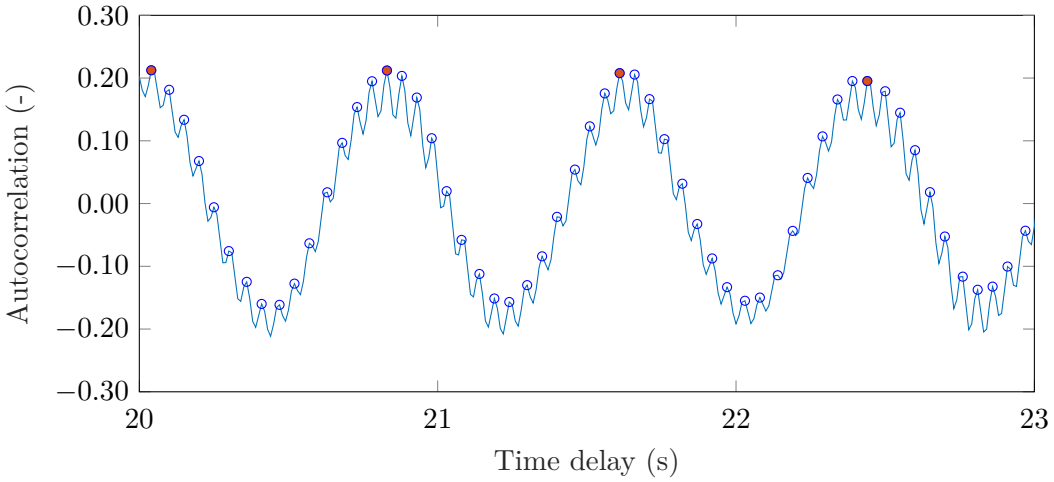

Figure 8-5: Part of autocorrelation graph of load case: four loaded legs under an angle of 15.3°, by ice approaching with a velocity of 0.385 m s^{-1}, using modal damping. This load case lies in the continuous brittle crushing regime. Next to the fundamental frequency of 1.245 Hz (indicated by red dots), a higher frequency is present in the autocorrelation (indicated by blue circles).

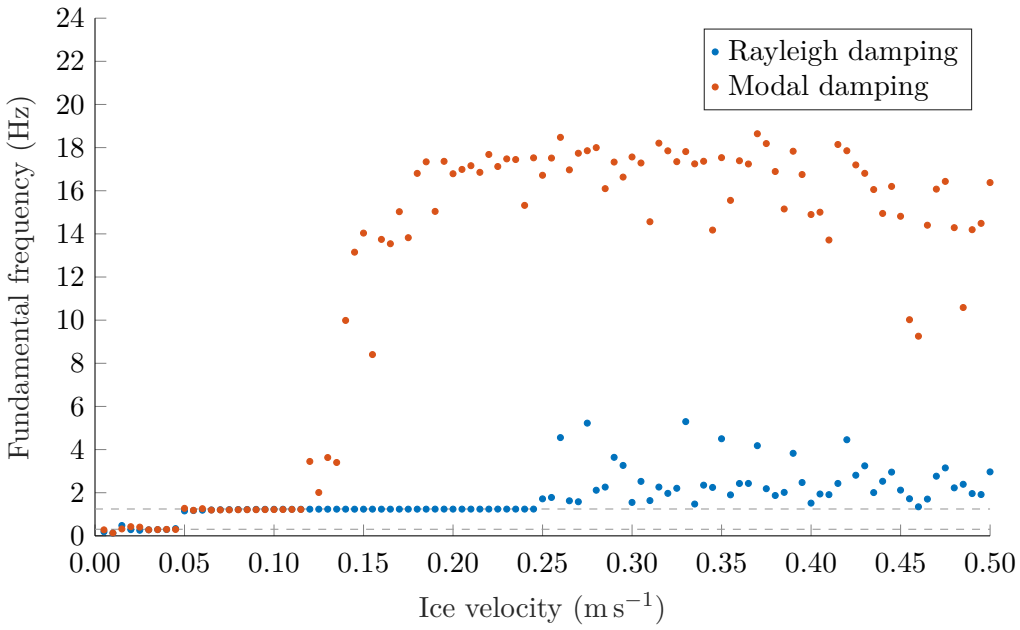

Figure 8-6: Plot of high frequency content of autocorrelation function versus ice velocity for two types of damping: Rayleigh damping and modal damping. The Rayleigh damping is scaled for the first and third mode to 1 %, for modal damping, the damping of all modes is set to 1 %. Here, four legs were loaded under an angle of 15.3°. The frequencies in the continuous brittle crushing regime mainly lie between 17 and 19 Hz.

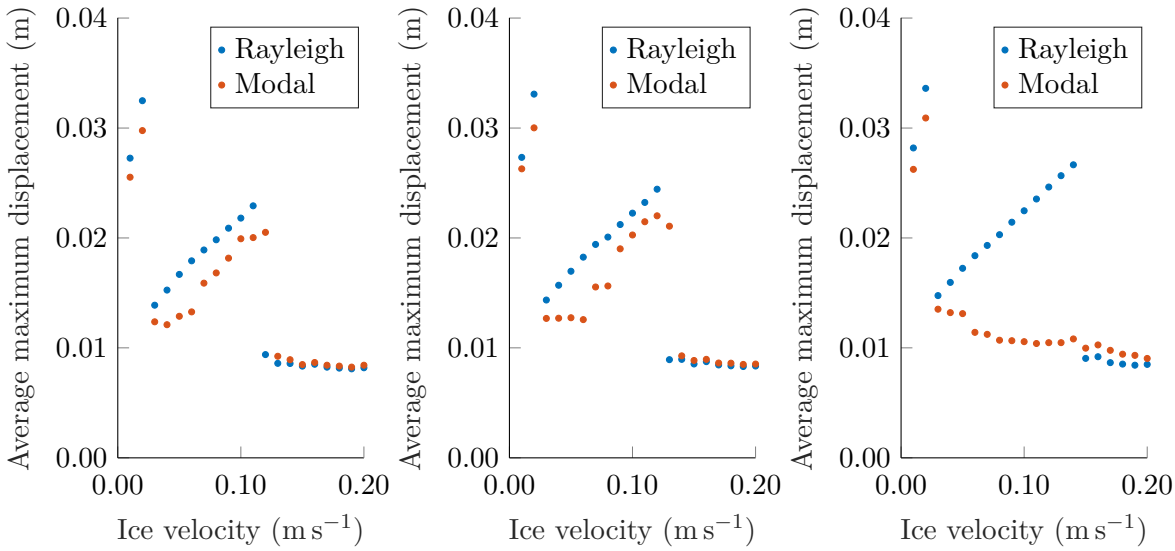

(a) Modes up to 15 Hz. **(b)** Modes up to 17 Hz. **(c)** Modes up to 18 Hz.

Figure 8-7: Maximum displacement of the structure with modes up to 15, 17 and 18 Hz. When incorporating modes up to 17 Hz, frequency lock-in occurs in both Rayleigh damping (blue) and modal damping (red) cases. However, when including modes up to 18 Hz, it is significantly distorted when using modal damping.

8-3 Effect of angle of approach

The effect of angle of approach on the occurrence of ice-induced vibrations (IIV) is studied by performing simulations where four legs are loaded, ranging the ice angle from 15.3° to 34.2°, as sketched in Figure 6-1a, for ice thicknesses of 0.3, 0.4 and 0.5 m. The average maximum displacement as a function of ice velocity for these load cases is plotted in Figure 8-8.

As shown in the figure, the data points are grouped per ice thickness, forming the three distinct lines as seen earlier in Figure 8-1. This implies that the angle of incidence has no effect on the occurrence of IIV when the structure is hit by the ice over the full width; it only determines how many legs are loaded by the ice. This is probably due to the fact that the modeled structure is symmetric. Due to linearity of the model, superposition of modes can be used to obtain the structural behavior in an arbitrary direction. Therefore, the resulting dynamics is the same for each angle of approach.

However, as discussed in Section 6-1, the rotational mode could be excited when only one leg is hit by the ice. This is simulated by applying an ice force to only one leg, at an angle of 45°. The results are shown in the next section.

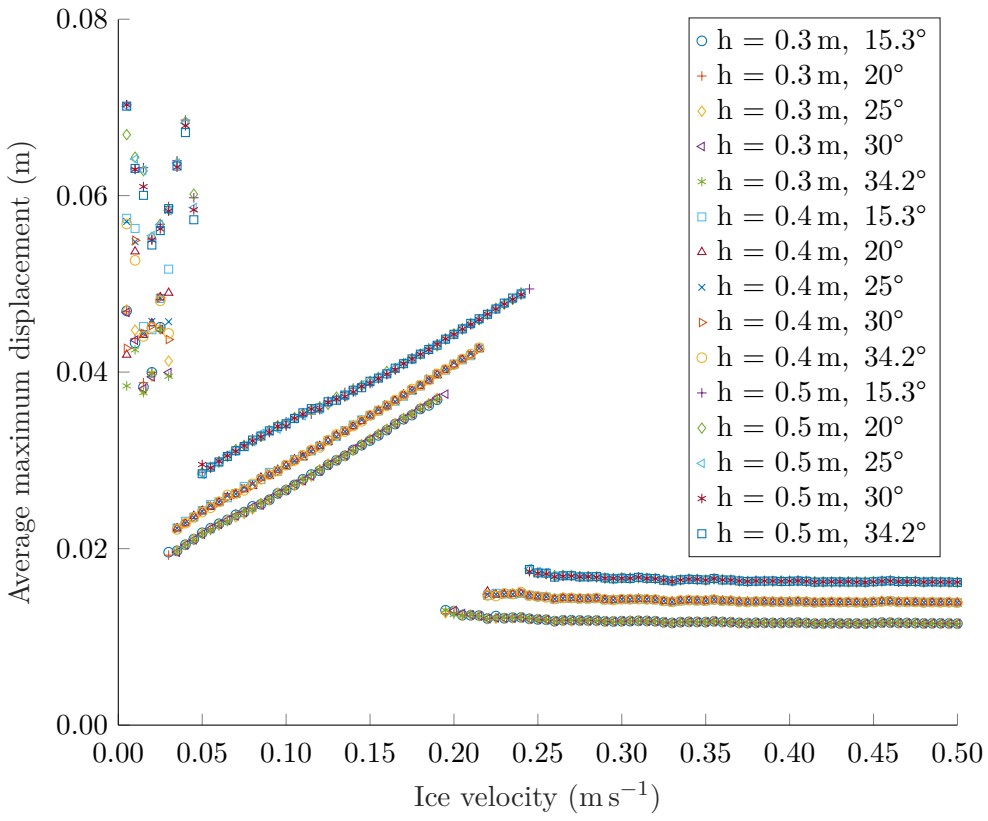

Figure 8-8: Graph of average maximum displacement versus ice velocity for the case where all four legs are loaded and the Rayleigh damping model is used. The angle of approach is varied from 15.3° to 34.2°, for ice thicknesses of 0.3, 0.4 and 0.5 m.

8-4 Rotational mode

The average maximum displacement and the fundamental frequency for the case where one leg is loaded in 45° are plotted in Figures 8-9 and 8-10, respectively.

As seen in the figures, frequency lock-in occurs for this load case, in the structural eigenmode of 1.245 Hz, as before. However, the rotational mode of 3.057 Hz does not appear in the plot of the fundamental frequency. In addition, the frequency of the rotational mode is not present in the Fast Fourier Transform of the displacement signals for both the Rayleigh damping and modal damping cases. It is therefore concluded that the rotational mode is not susceptible to frequency lock-in for this range of ice velocities.

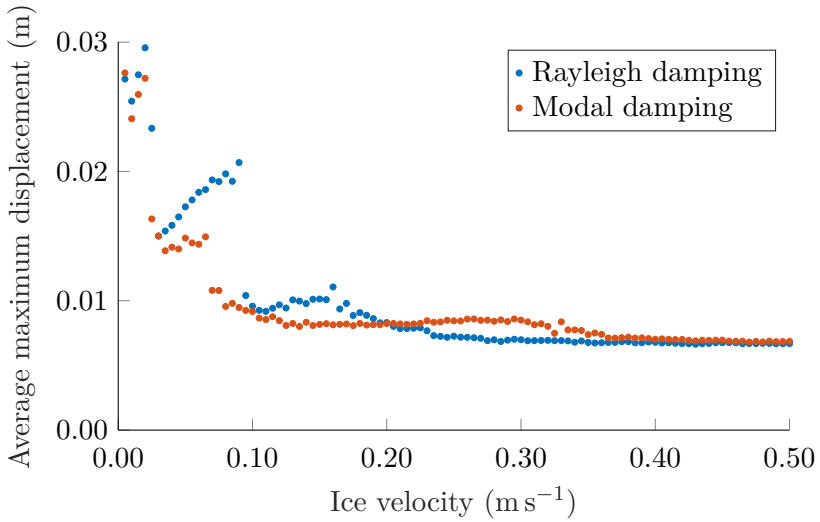

Figure 8-9: Graph of average maximum displacement versus ice velocity when only one leg is loaded by ice, under an angle of 45°, to test whether the rotational mode can be excited.

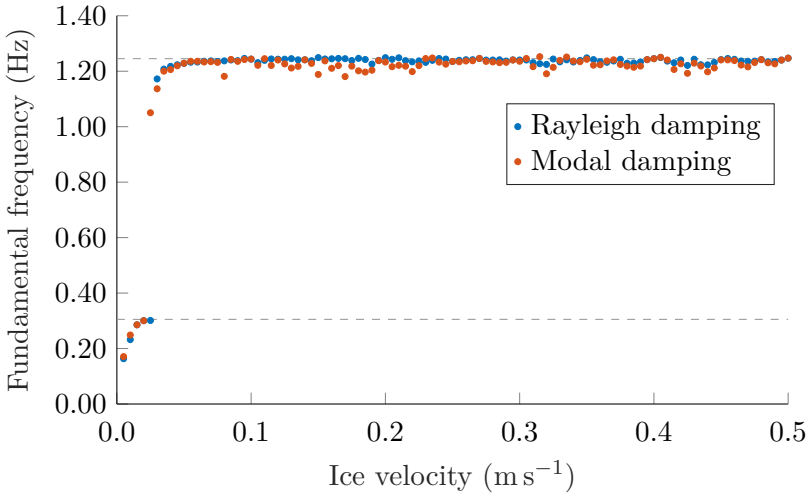

Figure 8-10: Graph of fundamental frequency versus ice velocity when only one leg is loaded by ice, under an angle of 45°.

8-5 Worst case scenarios of ice-only load cases

As concluded from the load cases above, the worst case scenario for the displacements at sea level due to ice loading in this study is the one in which four legs are in contact with ice of 0.5 m thick, modeled with Rayleigh damping. In Figure 8-8 it can be seen that the displacements at sea level are largest for the ice velocities $0.005\,\mathrm{m\,s^{-1}}$ and $0.245\,\mathrm{m\,s^{-1}}$, in the intermittent crushing and frequency lock-in regime respectively, from the simulation of ice approaching from 15.3°. The time series of the displacements are shown in Figures 8-11 and 8-12 for intermittent crushing and in Figures 8-13 and 8-14 for frequency lock-in. The average maximum displacement for $v_{\mathrm{ice}} = 0.005\,\mathrm{m\,s^{-1}}$ is 0.07 m and for $v_{\mathrm{ice}} = 0.245\,\mathrm{m\,s^{-1}}$ is 0.05 m. The maximum velocity of $v_{\mathrm{ice}} = 0.245\,\mathrm{m\,s^{-1}}$ for which FLI exists is considerably higher than the $0.1\,\mathrm{m\,s^{-1}}$ as stated by the International Organization for Standardization (ISO).

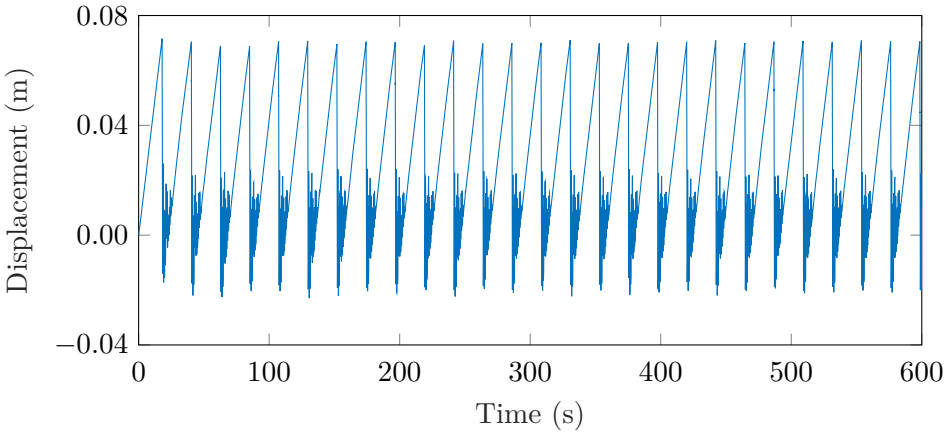

Figure 8-11: Full displacement time series for the load case of approaching ice of 0.5 m thick, loading four legs under 15.3° and ice velocity of $0.005\,\mathrm{m\,s^{-1}}$, which is in the IC regime.

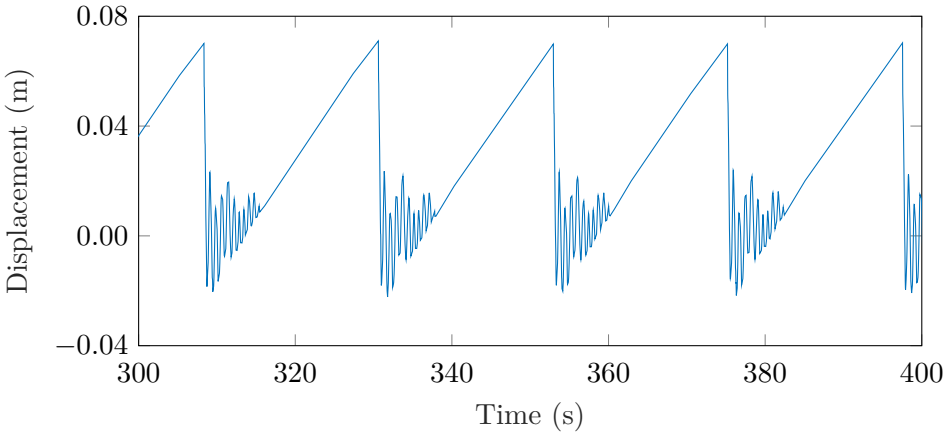

Figure 8-12: Part of the displacement time series for the load case of approaching ice of 0.5 m thick, loading four legs under 15.3° and ice velocity of $0.005\,\mathrm{m\,s^{-1}}$, which is in the IC regime.

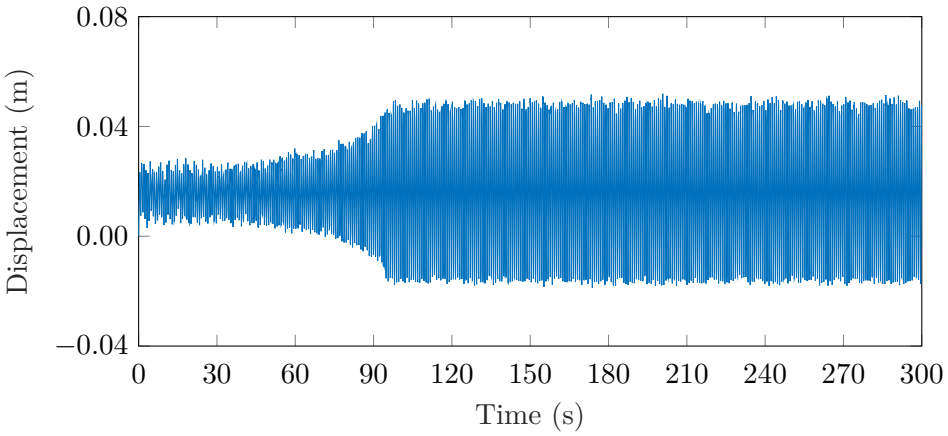

Figure 8-13: Displacement time series for the load case of approaching ice of 0.5 m thick, loading four legs under 15.3° and ice velocity of 0.245 m s^{-1}, which is in the FLI regime. The onset of FLI is visible in the first 100 seconds of the simulation.

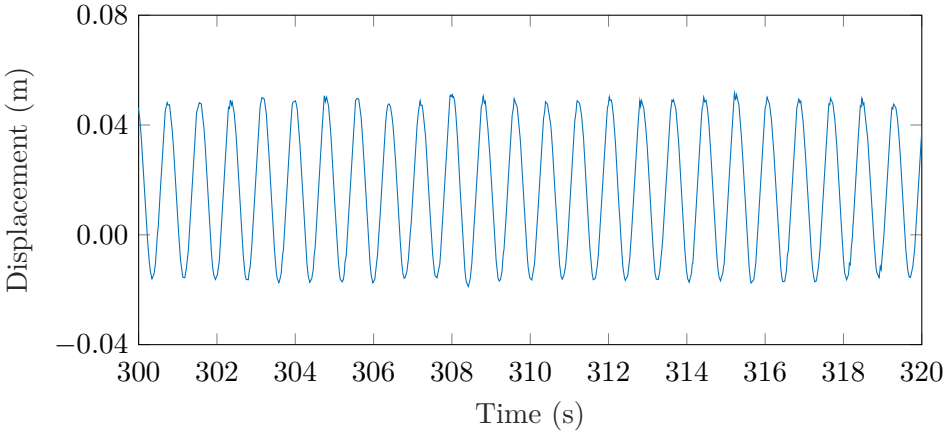

Figure 8-14: Displacement time series for the load case of approaching ice of 0.5 m thick, loading four legs under 15.3° and ice velocity of 0.245 m s^{-1}, which is in the FLI regime.

The same post-process is done to the node at tower top, where the large mass of the RNA is located. The average maximum displacement as a function of ice velocity is plotted in Figure 8-15.

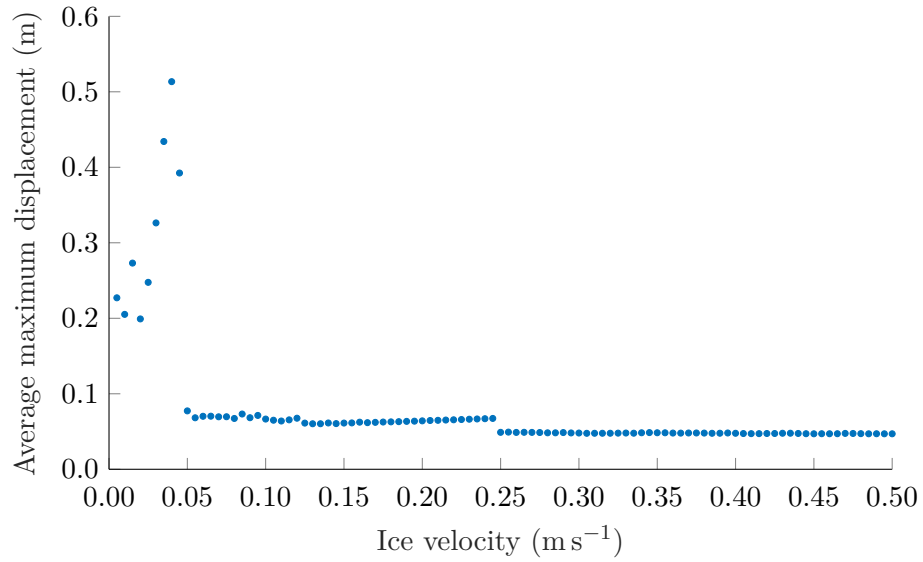

Figure 8-15: Graph of the average of the maximum displacement versus the ice velocity at the RNA for the worst case scenario: four loaded legs under 15.3°.

It is evident that the largest displacement of the RNA occurs for an ice velocity of 0.040 m s^{-1}. The average maximum displacement of the RNA is 0.51 m for this load case. To illustrate, the displacement graph for the first 100 seconds is depicted in Figure 8-16. The displacements in the frequency lock-in regime are relatively low, around 0.06 m, which is logical when looking at the FRF of the RNA in Appendix C. In the figure can be seen that the output displacement at tower top due to a sinusoidal input in the frequency of the second eigenmode is relatively small. This is due to the lower modal displacement of the second eigenmode at the tower top.

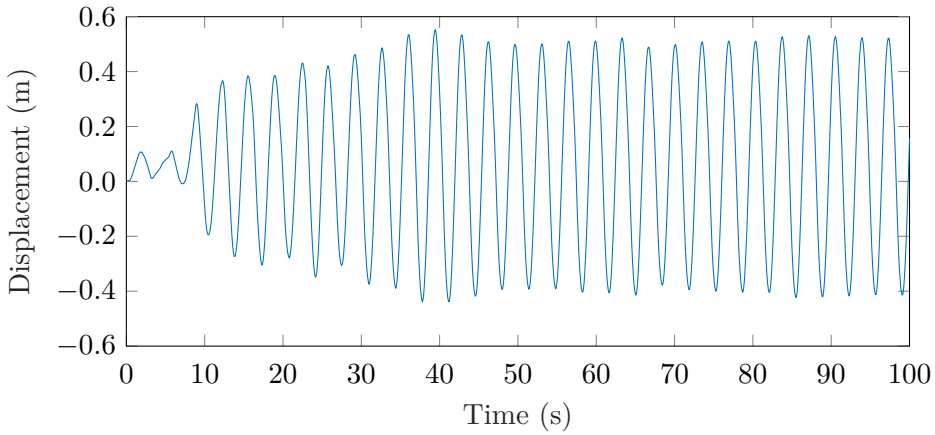

Figure 8-16: Time series of displacement of the RNA for the worst case scenario: four loaded legs under 15.3° and an ice velocity of 0.040 m s^{-1}. The RNA oscillates at the first eigenfrequency.

8-6 Effect of aerodynamic loading

The maximum displacements for the load case where four legs are loaded by ice, and the RNA is loaded by a thrust force due to both a cut-in and rated wind speed are plotted in Figure 8-17. It turns out that the occurrence of IIV, as measured at water level, is not affected by the aerodynamic force; the three regimes are still observed in the graph and a distortion is not apparent. Moreover, when comparing the graph for maximum displacements with aerodynamic force with the average displacement without wind force (plotted in yellow in Figure 8-17), the maximum displacements have increased. The largest average maximum displacement at sea level is 0.07 m for an ice velocity of $0.240\,\mathrm{m\,s^{-1}}$, when a thrust force is applied at rated wind speed.

The maximum displacement at the RNA versus ice velocity is plotted in Figure 8-18. As can be seen from the figure, the maximum displacement of the RNA is 0.98 m for an ice velocity of $0.040\,\mathrm{m\,s^{-1}}$. Part of the displacement graph is depicted in Figure 8-19.

However, care should be taken while interpreting these results, because the aerodynamic damping is neglected, which can have a considerable effect on the dynamics of the structure. Simulations with the simplified aerodynamic damping, as described in Section 6-2, result in Figure 8-20. As can be seen, the displacements in the IC regime are slightly larger compared to the case without aerodynamic damping, but the main difference is the fact that the length of the FLI regime is much shorter. This is attributed to the higher damping of the second eigenmode, compared to the higher modes. Moreover, the displacements of the RNA are lower compared to the case without aerodynamic damping, as can be seen in Figure 8-21.

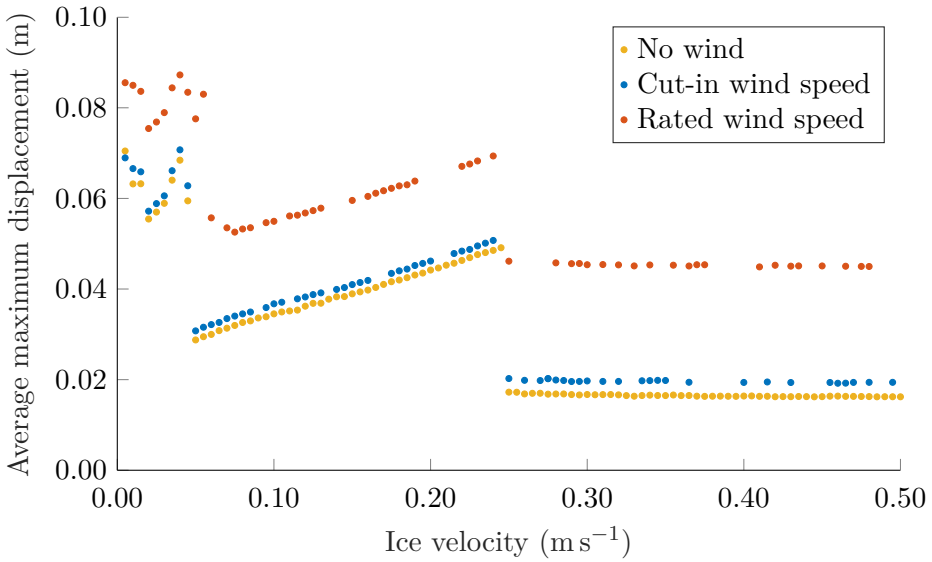

Figure 8-17: Maximum displacement at sea level versus ice velocity, without wind force and when a thrust force time series at cut-in wind speed ($3\,\mathrm{m\,s^{-1}}$) and rated wind speed ($12\,\mathrm{m\,s^{-1}}$) are applied to the RNA, without aerodynamic damping. Not all data points are present, since several simulations did not finish, probably since a smaller time step was necessary to solve for the fast fluctuating thrust force.

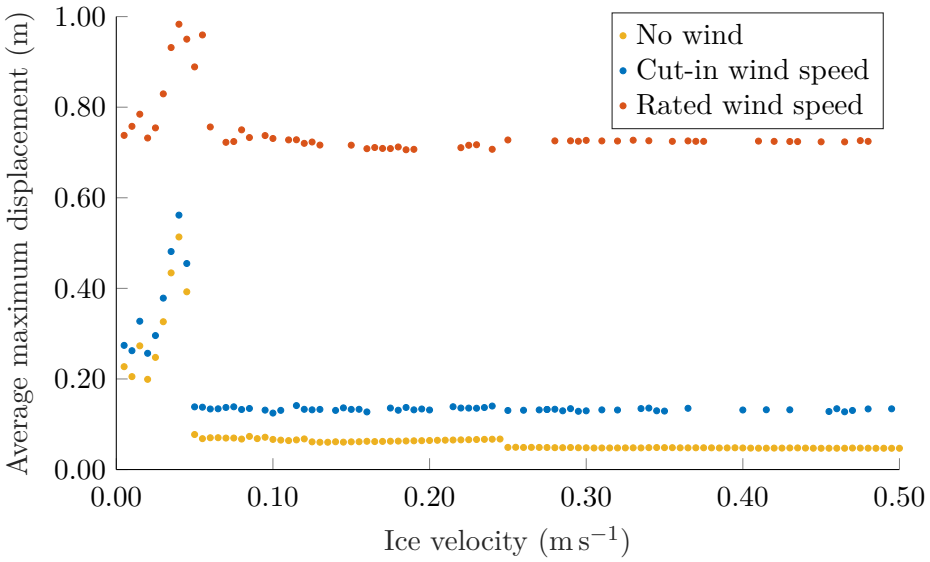

Figure 8-18: Maximum displacement at tower top versus ice velocity, when a thrust force time series at cut-in wind speed ($3\,m\,s^{-1}$) and rated wind speed ($12\,m\,s^{-1}$) are applied to the RNA, without aerodynamic damping.

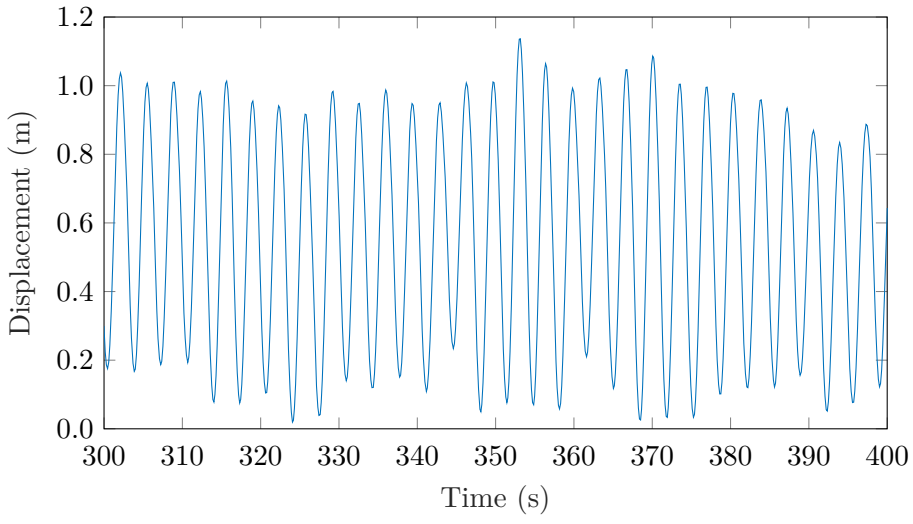

Figure 8-19: Time series of displacement of the RNA, when a thrust force time series at rated wind speed ($12\,m\,s^{-1}$) is applied to the RNA, without aerodynamic damping, and ice hits the structure at $0.040\,m\,s^{-1}$.

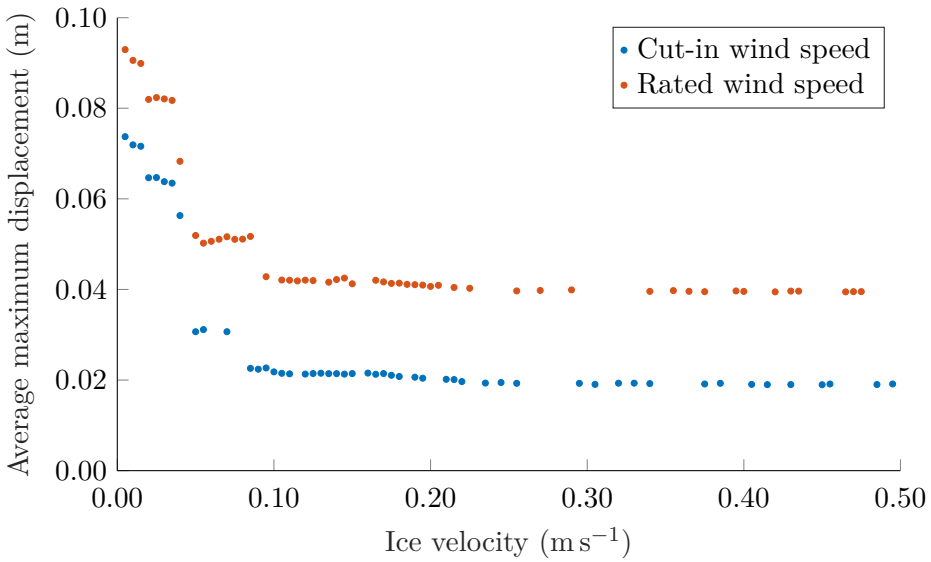

Figure 8-20: Maximum displacement at sea level versus ice velocity, when a thrust force time series at cut-in wind speed (3 m s^{-1}) and rated wind speed (12 m s^{-1}) are applied to the RNA, with aerodynamic damping.

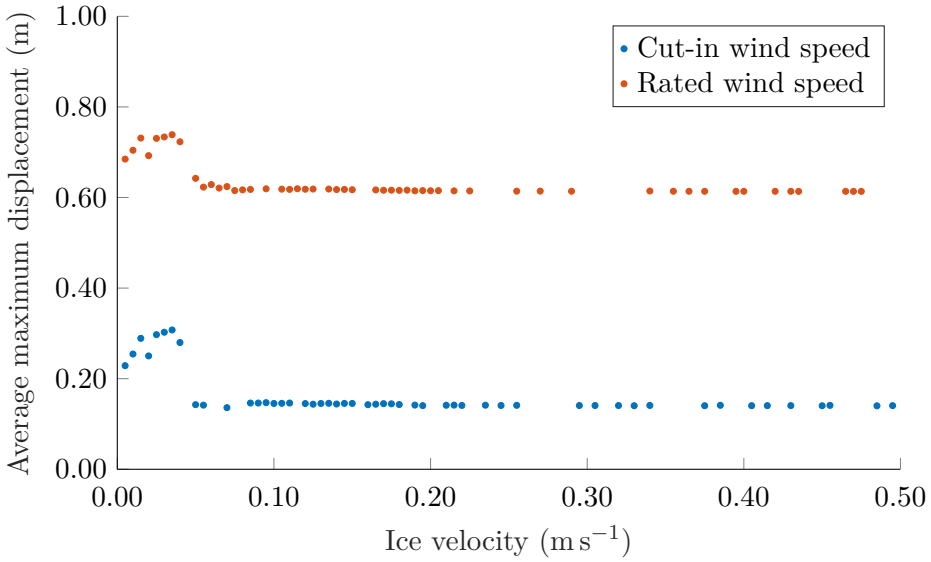

Figure 8-21: Maximum displacement at tower top versus ice velocity, when a thrust force time series at cut-in wind speed (3 m s^{-1}) and rated wind speed (12 m s^{-1}) are applied to the RNA, with aerodynamic damping.

Chapter 9

Conclusions and recommendations

The goal of this research was to identify the occurrence of ice-induced vibrations (IIV) in offshore wind turbines with a jacket foundation. To this end, the Offshore Code Comparison Collaboration Continuation (OC4) reference turbine model was implemented in MATLAB. The resulting model was compared to other implementations of the OC4 structure in literature and has shown to be in good agreement. Using this structural model, the eigenmodes were computed and by plotting the frequency response function (FRF) an estimation of the susceptibility of the eigenmodes to frequency lock-in (FLI) was made. The second eigenmode has shown to have a relatively large displacement at sea level, the point where the ice force acts on the structure, and is therefore most susceptible to FLI.

Then, the phenomenological ice model as published by Hendrikse et al. (2018) was implemented and the coupling with the structural model was realized. As the ice model is described in the time domain and the structural model in the modal domain, the coupling required switching between the two domains, which was successfully developed and implemented. To reduce the simulation time, the structural modes with a high frequency were disregarded. This coupling framework can also be used in other fields of interest, where a physical displacement needs to be extracted from a model which is in de modal domain.

9-1 Conclusions

Several load cases were simulated using the coupled model. Graphs of maximum displacement and fundamental frequency are presented to determine the occurrence of IIV as a function of ice velocity. This approach is new with respect to the existing approach for a one degree-of-freedom structural model, where the structural velocity is used as a measure for frequency lock-in. It was revealed that IIV do occur in the model of the offshore wind turbine and the second eigenmode is indeed excited in FLI.

Afterwards, the influence of the ice thickness on the IIV regimes was studied. It was shown that thicker ice induces larger displacements due to higher forces. Moreover, the thickness has shown to affect the range of ice velocities at which the FLI regime occurs. The regime extends

to higher ice velocities for thicker ice, exceeding the maximum ice velocity of $0.15\,\mathrm{m\,s^{-1}}$ as stated by Kärnä et al. (2013).

Simulations using two different damping models, Rayleigh damping and modal damping, have revealed that the chosen structural damping model influences the structural displacement considerably. In case of Rayleigh damping, the FLI regime continues for higher ice velocities, while it is terminated earlier when modal damping is applied. This effect is contributed to the excitation of higher structural modes in the modal damping case, which distort the lock-in. These have less effect in the Rayleigh damping case, leading to a longer lock-in regime. Thus, application of structural damping should be chosen carefully. Using the modal damping model for the OC4 wind turbine, as proposed by Vorpahl et al. (2013), could not reveal the worst case scenario due to IIV.

The angle of approach of the ice has shown to have no effect on the IIV in the simulations. The resulting displacements are the same for all angles of approaching ice. This is due to the fact that the model of the wind turbine is symmetric. Moreover, using an asymmetric load case, the rotational eigenmode of the structure was not excited. The angle of approach only determines how many legs of the structure experience an ice force, due to shielding.

Next, simulations are performed with an aerodynamic force acting on the rotor and nacelle assembly (RNA). The results without aerodynamic damping revealed that the occurrence of IIV was not distorted, the FLI regime was even extended to larger velocities. Moreover, the displacement of the RNA in this case was larger than in previous simulations. However, by adding the aerodynamic damping values in the model, it was shown that the FLI regime was considerably shorter and the RNA displacements were less.

Overall, it is concluded that IIV can occur in this model of an offshore wind turbine with a jacket support structure, resulting in significant vibrations. According to the performed ice-only load cases, the case where the four legs were loaded was the worst case scenario. Adding the thrust force, without adding aerodynamic damping, resulted in even larger displacements at both water level and the tower top.

Concluding, the effect of these IIV should be considered in the design phase of an offshore wind turbine with a jacket support structure. The presented modeling framework can be used to determine the occurrence of IIV of other offshore structures in ice infested areas as well.

9-2 Recommendations

Finally, several recommendations for future research or extension of this project are proposed.

First of all, the ice model could be extended to also incorporate splitting, bending failure and the formation of ice rubble. Since ice cones are already being placed on jacket legs to prevent ice-induced vibrations, it will be interesting to study their effect on the resulting structural dynamics while interacting with ice, using both the out-of-plane bending failure and splitting behavior. In addition, it is not yet clear what the effect of ice rubble can be. In the worst case, it accumulates between the legs of the jacket structure, increasing the ice force.

Moreover, the ice model could be extended to two dimensions, accounting for its effect on the structural motion perpendicular to the ice velocity. When taking into account the shape of the structure, the direction of the net ice force can be simulated. As Willems (2016)

and Hendrikse (2017) already stated, further validation of the ice model could be done by performing full-scale experiments.

The second set of recommendations regard the structural side. The structural model will be more accurate when more features are included. The RNA is modeled as point mass, but the dynamic model will be more accurate when the blades are incorporated. Then, the structural model will be asymmetric, and the angle of approaching ice could have an effect on the resulting motion. Moreover, the thrust force and aerodynamic damping can then be incorporated in the model as a function of the blade motion. Furthermore, the braces at water level were not taken into account in the interaction with ice; they were modeled as if they were moving in air. However, the braces can have an effect on the local dynamics of the structure. They also need to be incorporated when splitting is added to the ice model.

As stated before, care should be taken when applying a structural damping model. More testing is required to compute the higher damping coefficients, which are important for the occurrence of IIV. This also holds for the aerodynamic damping.

Having a complete ice and structural model, the ultimate goal would be to perform coupled simulations with wind, wave and ice loading and including the soil-structure interaction to assess the worst case scenarios. Using the simulations, a fatigue analysis can be performed to assess the impact of the cyclic loading during IIV. Moreover, the effect of the high forces during intermittent crushing (IC) can be studied to assess the ultimate state of the structure.

Then, using the structural model, the designer can change structural parameters in order to try to avoid or reduce the IIV. For example, the placement of braces can influence the local modes at water level. Using the knowledge that these can disturb the IIV, designing the braces in an innovative way can contribute. Moreover, one can play with the mass, damping and stiffness distributions to alter the eigenmodes and eigenfrequencies which are susceptible to IIV.

From a practical point of view, an estimation of the occurrence of IIV based on structural and ice properties would be profitable. In addition, automatic categorization of the IIV regime based on the displacement time series solely would be time saving, as the parameter sweep over the ice velocity is no longer required.

Appendix A

Orthogonality of eigenmodes

Consider two different solutions of Equation 5-1:

$$\mathbf{K}\boldsymbol{\phi}_r = \omega_r^2 \mathbf{M}\boldsymbol{\phi}_r, \tag{A-1}$$
$$\mathbf{K}\boldsymbol{\phi}_s = \omega_s^2 \mathbf{M}\boldsymbol{\phi}_s. \tag{A-2}$$

Pre-multiplying these equations by $\boldsymbol{\phi}_s^\mathsf{T}$ and $\boldsymbol{\phi}_r^\mathsf{T}$ respectively, yields:

$$\boldsymbol{\phi}_s^\mathsf{T}\mathbf{K}\boldsymbol{\phi}_r = \omega_r^2 \boldsymbol{\phi}_s^\mathsf{T}\mathbf{M}\boldsymbol{\phi}_r, \tag{A-3}$$
$$\boldsymbol{\phi}_r^\mathsf{T}\mathbf{K}\boldsymbol{\phi}_s = \omega_s^2 \boldsymbol{\phi}_r^\mathsf{T}\mathbf{M}\boldsymbol{\phi}_s. \tag{A-4}$$

Using the property of symmetric matrices:

$$\boldsymbol{x}^\mathsf{T}\mathbf{A}\boldsymbol{y} = \boldsymbol{y}^\mathsf{T}\mathbf{A}\boldsymbol{x}, \tag{A-5}$$

equation A-3 can be rewritten as:

$$\boldsymbol{\phi}_r^\mathsf{T}\mathbf{K}\boldsymbol{\phi}_s = \omega_r^2 \boldsymbol{\phi}_r^\mathsf{T}\mathbf{M}\boldsymbol{\phi}_s, \tag{A-6}$$

since $\mathbf{K}$ and $\mathbf{M}$ are symmetric by definition. Subtracting equation A-6 from A-4 results in:

$$\left(\omega_s^2 - \omega_r^2\right) \boldsymbol{\phi}_r^\mathsf{T}\mathbf{M}\boldsymbol{\phi}_s = 0. \tag{A-7}$$

Since the term $(\omega_s^2 - \omega_r^2)$ is nonzero for $r \neq s$ (with distinct eigenfrequencies ω_s and ω_r), it is concluded that

$$\boldsymbol{\phi}_r^\mathsf{T}\mathbf{M}\boldsymbol{\phi}_s = 0. \tag{A-8}$$

Substituting this result back into equation A-6 yields

$$\boldsymbol{\phi}_r^\mathsf{T}\mathbf{K}\boldsymbol{\phi}_s = 0. \tag{A-9}$$

Properties A-8 and A-9 are referred to as mass-orthogonality and stiffness-orthogonality of the eigenmodes.

Appendix B

Higher structural modes

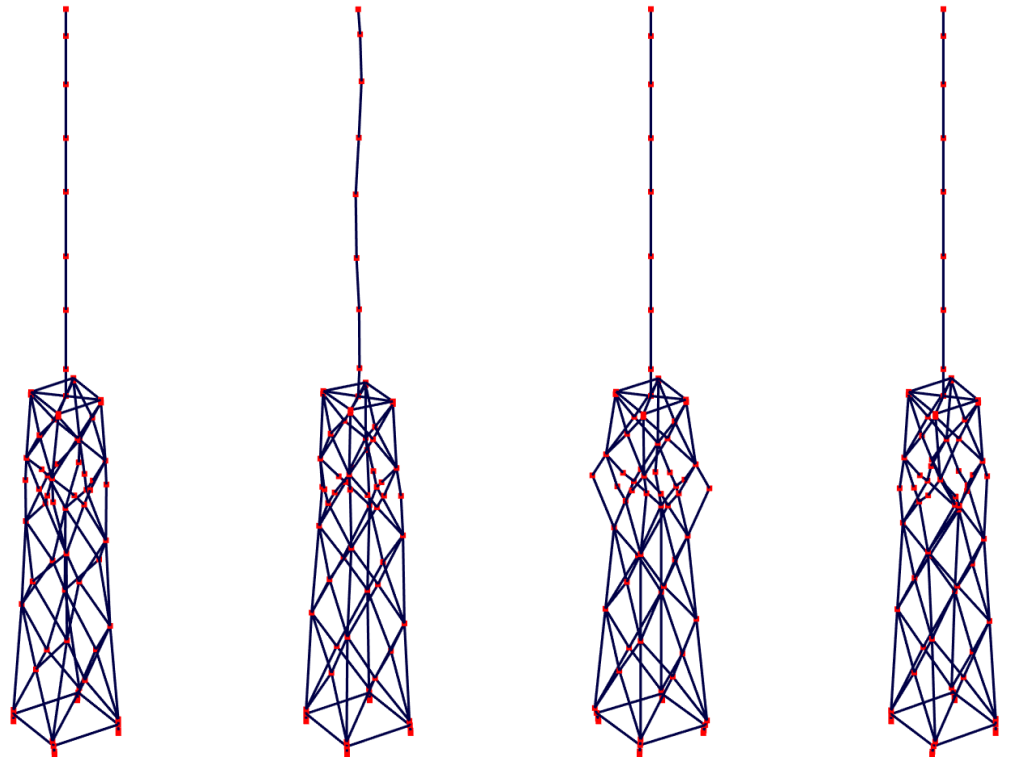

(a) Mode 40
17.154 Hz

(b) Mode 41
17.868 Hz

(c) Mode 43
18.388 Hz

(d) Mode 44
19.194 Hz

Figure B-1: Graphic representation of the eigenmodes of the structure from 17 to 21 Hz.

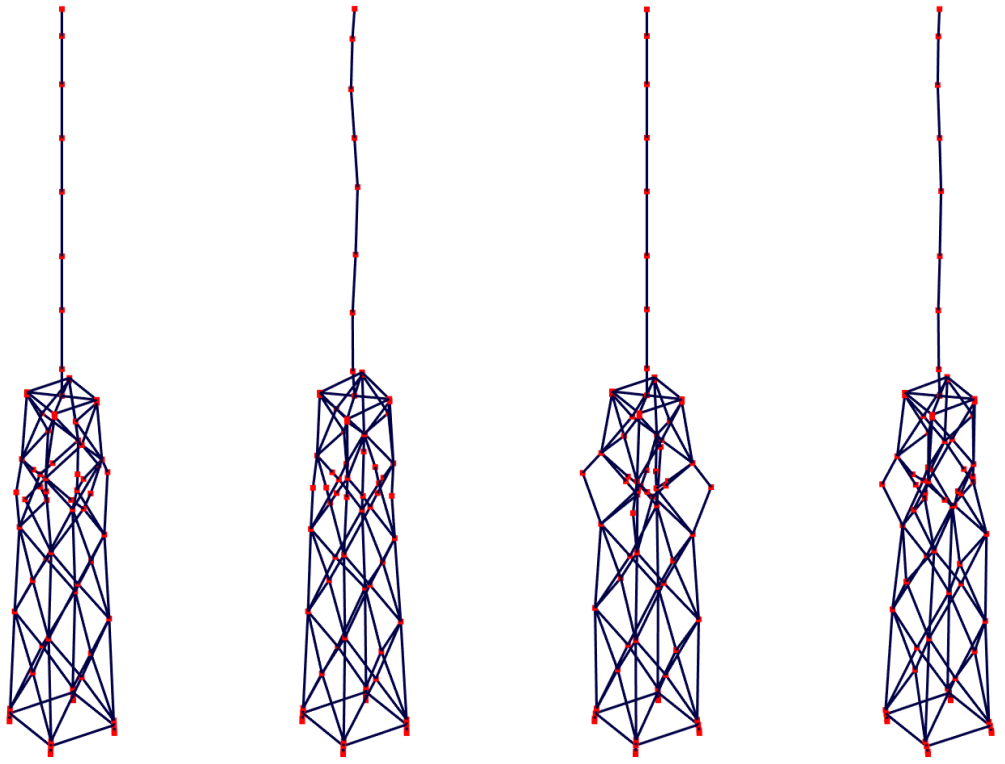

(e) Mode 45
19.201 Hz

(f) Mode 46
19.458 Hz

(g) Mode 48
19.604 Hz

(h) Mode 49
20.319 Hz

Figure B-1: Graphic representation of the eigenmodes of the structure from 17 to 21 Hz.

Appendix C

Frequency response function RNA

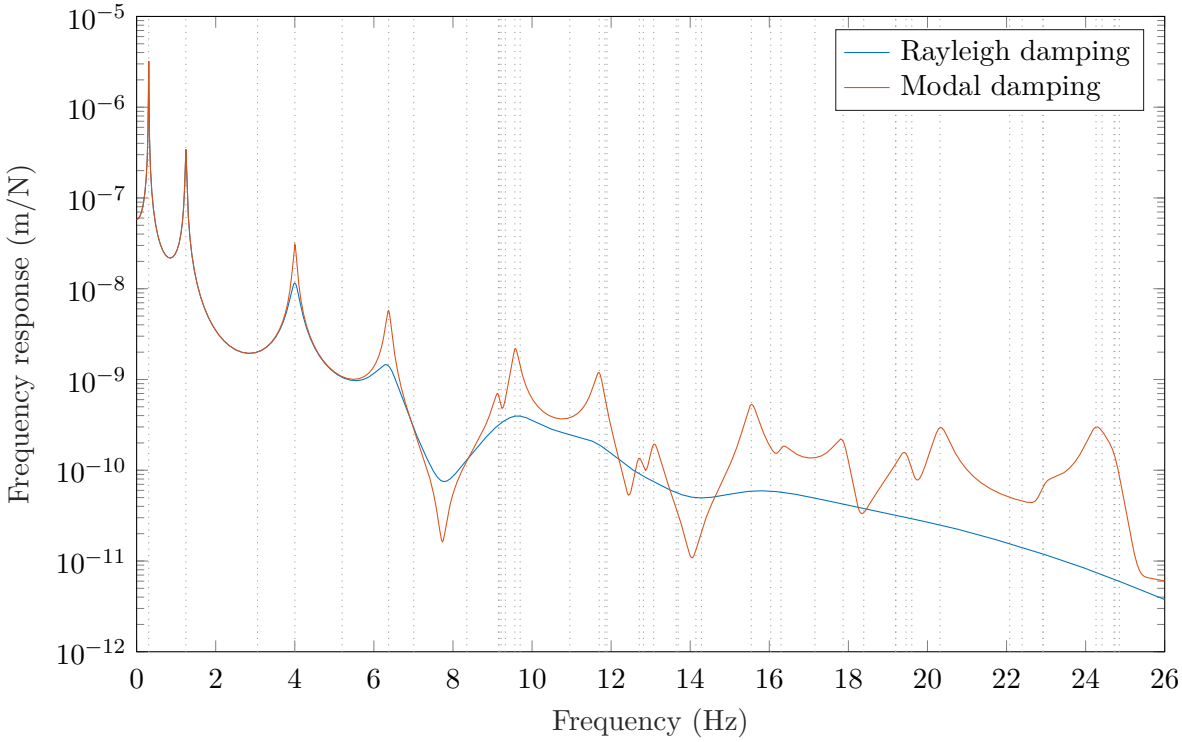

Figure C-1: Graph of the frequency response function using two different damping models. Nodes 44 and 47 are loaded sinusoidally in-phase and the output at node 73 is plotted (at the top of the structure). As can be seen, the damping in the modal damping model is lower compared to the Rayleigh damping case.

Bibliography

M.F. Ashby, A.C. Palmer, M. Thouless, D.J. Goodman, M. Howard, S.D. Hallam, S.A.F. Murrell, N. Jones, T.J.O. Sanderson, and A.R.S. Ponter. Nonsimultaneous Failure and Ice Loads on Arctic Structures. In *Proceedings of the 18th Annual Offshore Technology Conference*, pages 399–404, 1986.

Mehmet Bilgili, Abdulkadir Yasar, and Erdogan Simsek. Offshore wind power development in Europe and its comparison with onshore counterpart. *Renewable and Sustainable Energy Reviews*, 15(2):905–915, 2011.

BINE Information Service. Wind turbine technology and components. URL http://www.bine.info/en/publications/publikation/rave-forschen-am-offshore-testfeld/anlagentechnik-und-komponenten/?type=333.

Denis Blanchet, Archie Chrucher, John Fitzpatrick, and Paulette Badra-Blanchet. An analysis of observed failure mechanisms for laboratory first year and multi-year ice, 1988.

K.A. Blenkarn. Measurement and Analysis of Ice Forces on Cook Inlet structures. In *Offshore Technology Conference*, pages 364–375, 1970.

Anil K. Chopra. *Dynamics of Structures: Theory and Applications to Earthquake Engineering*. Pearson Education, 2015.

Antonio Colmenar-Santos, Javier Perera-Perez, David Borge-Diez, and Carlos Depalacio-Rodríguez. Offshore wind energy: A review of the current status, challenges and future development in Spain. *Renewable and Sustainable Energy Reviews*, 64:1–18, 2016.

Robert D. Cook, David S. Malkus, Michael E. Plesha, and Robert J. Witt. *Concepts and applications of finite element analysis*. John Wiley & Sons, 2012.

Claude Daley. Ice edge contact and failure. *Cold Regions Science and Technology*, 21(1):1–23, 1992.

M. Damgaard, L.B. Ibsen, L.V. Andersen, and J.K.F. Andersen. Cross-wind modal properties of offshore wind turbines identified by full scale testing. *Journal of Wind Engineering and Industrial Aerodynamics*, 116:94–108, 2013.

J.P. Dempsey, A.C. Palmer, and D.S. Sodhi. High pressure zone formation during compressive ice failure. *Engineering Fracture Mechanics*, 68(17-18):1961–1974, 2001.

Christof Devriendt, Pieter Jan Jordaens, Gert De Sitter, and Patrick Guillaume. Experimental and computational damping estimation of an offshore wind turbine on a monopile foundation. *Journal of Wind Engineering and Industrial Aerodynamics*, 120:96–106, 2013.

Esa Eranti. *Dynamic ice structure interaction - Theory and applications*. PhD thesis, Helsinki University of Technology, 1992.

Charbel Farhat, Philip Avery, Todd Chapman, and Julien Cortial. Dimensional reduction of nonlinear finite element dynamic models with finite rotations and energy-based mesh sampling and weighting for computational efficiency. *International Journal for Numerical Methods in Engineering*, 98(9):625–662, 2014.

Giancarlo Genta. *Introduction to the Mechanics of Space Robots*. Springer, 2012.

Michel Géradin and Daniel J. Rixen. *Mechanical Vibrations: Theory and Application to Structural Dynamics*. John Wiley & Sons, Ltd, 2015.

Helge Gravesen and Tuomo Kärnä. Ice Loads for Offshore Wind Turbines in Southern Baltic Sea. In *Proceedings of the 20th International Conference on Port and Ocean Engineering under Arctic Conditions*, number August, 2009.

H. Hendrikse, G. Ziemer, and C.C. Owen. Experimental validation of a model for prediction of dynamic ice-structure interaction. *Cold Regions Science and Technology*, 151:345–358, 2018.

Hayo Hendrikse. *Ice-induced vibrations of vertically sided offshore structures*. PhD thesis, 2017.

Hayo Hendrikse and Andrei V. Metrikine. Interpretation and prediction of ice induced vibrations based on contact area variation. *International Journal of Solids and Structures*, 75-76:336–348, 2015.

Hayo Hendrikse and Andrei V. Metrikine. Ice-induced vibrations and ice buckling. *Cold Regions Science and Technology*, 131:129–141, 2016.

Hayo Hendrikse, Frank W. Renting, and Andrei V. Metrikine. Analysis of the fatigue of offshore wind turbine generators under combined ice- and aerodynamic loading. In *International Conference on Ocean, Offshore and Arctic Engineering*, pages 1–10, 2014.

Guojun Huang and Pengfei Liu. A Dynamic Model for Ice-Induced Vibration of Structures. *Journal of Offshore Mechanics and Arctic Engineering*, 131(February):1–6, 2009.

Yan Huang, Qingzeng Shi, and An Song. Model test study of the interaction between ice and a compliant vertical narrow structure. *Cold Regions Science and Technology*, 49(2): 151–160, 2007.

IEC 61400-3:2009. Wind turbines – Part 3: Design requirements for offshore wind turbines, 2009.

ISO 19906. Petroleum and natural gas industries – Arctic offshore structures, 2010.

Xu Ji and Erkan Oterkus. A dynamic ice-structure interaction model for ice-induced vibrations by using Van der Pol equation. *Ocean Engineering*, 128(July):107–111, 2017.

J. Jonkman, S. Butterfield, W. Musial, and G. Scott. Definition of a 5-MW Reference Wind Turbine for Offshore System Development. Technical Report February, 2009.

T. Kärnä, H. Andersen, A. Gürtner, A. Metrikine, D. Sodhi, M. Loo, G. Kuiper, R. Gibson, D. Fenz, K. Muggeridge, C. Wallenburg, J-F. Wu, and M. Jefferies. Ice-induced vibrations of offshore structures – Looking beyond ISO 19906. In *Proceedings of the 22nd International Conference on Port and Ocean Engineering under Arctic Conditions*, pages 1–12, 2013.

Tuomo Kärnä and Risto Turunen. Dynamic response of narrow structures to ice crushing. *Cold Regions Science and Technology*, 17:173–187, 1989.

K.N. Korzhavin. *Action of Ice on Engineering Structures*. Publishing House of Siberian Branch of USSR Academy of Sciences, 1962.

Matti Leppäranta. An ice drift model for the Baltic Sea. *Tellus*, 6(1981):583–596, 1981.

Xiang Liu, Gang Li, Robert Oberlies, and Qianjin Yue. Research on short-term dynamic ice cases for dynamic analysis of ice-resistant jacket platform in the Bohai Gulf. *Marine Structures*, 22(3):457–479, 2009a.

Xiang Liu, Gang Li, Qianjin Yue, and Robert Oberlies. Acceleration-oriented design optimization of ice-resistant jacket platforms in the Bohai Gulf. *Ocean Engineering*, 36(17-18): 1295–1302, 2009b.

S. Løset, K. Shkhinek, and K.V. Høyland. *Ice physics and mechanics*. Norwegian University of Science and Technology (NTNU), 1998.

Mauri Määttänen. On conditions for the rise of self-excited ice-induced autonomous oscillations in slender marine pile structures. Technical report, University of Oulu, 1978.

Hudson Matlock, William P. Dawkins, and John J. Panak. A Model for the Prediction of Ice-Structure Interaction. In *First Offshore Technology Conference*, pages 687–694, 1969.

Andrei V. Metrikine. *Structural dynamics, notes lecture 8*. Faculty of Civil Engineering and Geosciences, Delft University of Technology, 2017.

Ari Muhonen. *Evaluation of three ice-structure interaction models*. PhD thesis, 1996.

David Newell. Implementing wind power policy - Institutional frameworks and the beliefs of sovereigns. *Land Use Policy*, 72:16–26, 2018.

Andrew Palmer and Ken Croasdale. *Arctic Offshore Engineering*. World Scientific Publishing, 2013.

Harold R. Peyton. Ice and Marine Structures, Part 2 – Sea Ice Properties. *Ocean Industry*, 3(9):59–65, 1968.

A.R.S. Ponter, A.C. Palmer, D.J. Goodman, M.F. Ashby, A.G. Evans, and J.W. Hutchinson. The force exerted by a moving ice sheet on an offshore structure – Part 1. The creep mode. *Cold Regions Science and Technology*, 8(2):109–118, 1983.

T.J.O. Sanderson. *Ice Mechanics: Risks to Offshore Structures*. Graham and Trotman, 1988.

Erland M. Schulson and Paul Duval. *Creep and Fracture of Ice*. Cambridge University Press, 2009.

Wei Shi, Xiang Tan, Zhen Gao, and Torgeir Moan. Numerical study of ice-induced loads and responses of a monopile-type offshore wind turbine in parked and operating conditions. *Cold Regions Science and Technology*, 123:121–139, 2016.

Devinder S. Sodhi. An ice-structure interaction model. *Mechanics of Geomaterial Interfaces*, 42:57–75, 1995.

Devinder S. Sodhi and Robert B. Haehnel. Crushing Ice Forces on Structures. *Journal of Cold Regions Engineering*, 17(4):153–170, 2003.

Takahiro Takeuchi, Masafumi Sakai, Satoshi Akagawa, Naoki Nakazawa, and Hiroshi Saeki. On the factors influencing the scaling of ice forces. In *IUAM Symposium on Scaling Laws in Ice Mechanics and Ice Dynamics*, pages 149–160, 2001.

G.W. Timco. Laboratory observations of macroscopic failure modes in freshwater ice. In *International Cold Regions Engineering Conference*, pages 605–614, 1991.

Maarten Vincent van der Seijs. *Experimental Dynamic Substructuring*. PhD thesis, 2016.

Paul L.C. van der Valk. *Coupled Simulations of Wind Turbines and Offshore Support Structures*. PhD thesis, 2014.

Sven N. Voormeeren, Paul L.C. van der Valk, Bas P. Nortier, David-Pieter Molenaar, and Daniel J. Rixen. Accurate and efficient modeling of complex offshore wind turbine support structures using augmented superelements. *Wind Energy*, 17(7):1035–1054, 2014.

Fabian Vorpahl, Wojciech Popko, and Daniel Kaufer. Description of a basic model of the 'UpWind reference jacket' for code comparison in the OC4 project under IEA Wind Annex 30. Technical report, 2013.

Shengyong Wang, Qianjin Yue, and Dayong Zhang. Ice-induced non-structure vibration reduction of jacket platforms with isolation cone system. *Ocean Engineering*, 70:118–123, 2013.

Yihe Wang, Leong Hien Poh, and Qianjin Yue. Reinvestigation of ice-induced vibrations of conical jacket structures using dimensionless parameters. *International Journal of Offshore and Polar Engineering*, 26(4):327–332, 2016.

W.F. Weeks. *On Sea Ice*. University of Alaska Press, 2010.

Johannes Weertman. Creep Deformation. *Annual Review of Earth and Planetary Sciences*, 11:215–240, 1983.

Tom Willems. Coupled modeling of dynamic ice-structure interaction on offshore wind turbines. 2016.

WindEurope. Wind energy in Europe: Outlook to 2020. Technical Report September, 2017. URL https://windeurope.org/about-wind/statistics/.

WindEurope. Wind in power 2017 - Annual combined onshore and offshore wind energy statistics, 2018.

M. Withalm and N.P. Hoffmann. Simulation of full-scale ice-structure-interaction by an extended Matlock-model. *Cold Regions Science and Technology*, 60(2):130–136, 2010.

Qianjin Yue, Fengwei Guo, and Tuomo Kärnä. Dynamic ice forces of slender vertical structures due to ice crushing. *Cold Regions Science and Technology*, 56, 2009.